BM@N Note
REC-2025-01.rev02, ANA-2025-01.rev02

Reconstruction and analysis of decays of strange particles produced in Xe+CsI interactions at $\sqrt{s_{NN}} = 3.26$ GeV with the BM@N detector

Roman Zinchenko[1], Julieta Drnoyan[1], Mikhail Kapishin[1], Igor Rufanov[1], Veronika Vasendina[1], Alexander Zinchenko[*,1], and Dmitry Zinchenko[1]

[1]Joint Institute for Nuclear Research, Joliot-Curie 6, Dubna 141980, Moscow region, Russia

October 9, 2026

Abstract

In December, 2022 - January, 2023 the BM@N experiment conducted its first physics run with full detector configuration. Over 500 million events of Xe beam interactions with CsI target with the beam kinetic energy of 3.8A GeV were collected.

Since then, strong efforts have been put to reconstruct the collected data and make preparations for physics analyses. The current status of such an activity related to reconstruction of strange particles weakly decayed to charged hadrons is presented in this paper. Main steps of the analysis procedure for a study of the strangeness production in nuclear collisions are outlined as well.

Реконструкция и анализ распадов странных частиц, рождённых во взаимодействиях Xe+CsI при энергии $\sqrt{s_{NN}} = 3.26$ ГэВ, в детекторе BM@N

Р.А. Зинченко, Д.Р. Дрноян, М.Н. Капишин, И.А. Руфанов, В.А. Васендина, А.И. Зинченко, Д.А. Зинченко

В декабре 2022 - январе 2023 г. эксперимент BM@N провёл первый физический сеанс с полной конфигурацией экспериментальной установки. Было записано более 500

*E-mail: Alexander.Zinchenko@jinr.ru

млн. событий взаимодействий пучка Xe с кинетической энергией 3.8A ГэВ с мишенью CsI.

С тех пор были приложены значительные усилия для реконструкции собранных данных и подготовки к физическому анализу. Текущий статус этой активности в области реконструкции странных частиц, распадающихся на заряженные адроны по слабому каналу, представлен в данной работе. Также описаны основные шаги процедуры анализа по изучению рождения странности в ядерных взаимодействиях.

1 Introduction

The experimental study of nuclear collisions in the energy range of several GeV per nucleon provides new information on the quantum chromodynamic (QCD) phase diagram at large baryon-chemical potentials, including the high-density equation-of-state (EOS) [1–4]. This is the main research subject of several ongoing and future experiments [5].

The Baryonic Matter at the Nuclotron (BM@N) at the NICA complex is one of such experiments. It carries out measurements with heavy ions at collision energies of $\sqrt{s_{NN}}$ = 2.3 - 3.3 GeV , where the highest net-baryon densities is created. In the last few years, the experiment performed several technical runs with light ions in partial detector configuration [6, 7]. The results obtained served as a proof of the detector concept, data processing and event reconstruction approaches. With the Booster startup at the end of 2020, the accelerator complex of the Booster and Nuclotron at JINR became capable of accelerating heavy-ion beams. The first physics run at the BM@N setup with Xe beam was performed in December, 2022 - January, 2023. Over 500 million events of Xe+CsI interactions with the Xe beam kinetic energy of 3.8A GeV ($\sqrt{s_{NN}}$ = 3.26 GeV) were collected.

Since then, the BM@N Colaboration worked hard to reconstruct the experimental data and properly tune the Monte Carlo simulation codes, i.e. to prepare for physics analyses on several topics. One of the most important items of the experimental program is a study of the strangeness production in nuclear collisions [8]. The current status of the activity in this research domain is presented in this paper. It demonstrates the detector performance for reconstruction of strange particle decays as well as shows the ability of the experiment to extract relevant physics observables, outlining the direction and steps of upcoming data analysis.

2 BM@N detector configuration

The layout of the BM@N setup in Xe+CsI run is presented in Fig. 1. Tracks of charged particles are reconstructed with the hybrid tracking system consisting of 4 stations of double-sided microstrip silicon sensors (Forward Silicon Detector) downstream from the single-layer target, located inside the Barrel Detector, and a set of 7 planes of GEM (gaseous electron multiplier) detectors with two-coordinate strip readout mounted downstream from the silicon stations. The Forward Silicon subsystem contains 6, 10, 14 and 18 detector modules in stations 1-4, respectively, arranged into pairs of half-stations below and above the beam line at a distance of $\sim$10 cm between stations. Each module with a width of 6 and a height of 12 cm (9 cm in the first station) has a strip pitch of 100 μm and a stereo angle, i.e. angle between strips on different sides, of 2.5°. The GEM detectors with a strip pitch of 800 μm and a stereo angle of 15° cover the region of $\pm$ $\sim$80 and $\pm$ $\sim$40 cm in horizontal (X-axis) and vertical (Y-axis) directions, respectively, and positioned at a distance of $\sim$30 cm from each other along the beam (Z-axis) below and above the beam pipe. Both the Forward Silicon and the GEM stations are installed inside a large aperture dipole magnet with a gap height of 1 m, providing a vertical magnetic field of up to 1.0 T in the magnet center. For different incoming beam rigidities, the magnetic field value is adjusted to steer the non-interacting beam particles through the vacuum beam pipe. For particle identification, the particle time-of-flight is measured with 2 walls of resistive plate chambers (mRPC) with strip readout, located at $\sim$4 m (TOF400) and $\sim$7 m (TOF700) downstream from the target. The Cathode Strip Chambers improve quality of spatial matching of reconstructed tracks with TOF measurements. The interaction centrality and event plane are characterized with the Forward Hadron Calorimeter. The interaction trigger is produced with the Barrel Detector, surrounding the target. More details on the BM@N detector systems can be found in Ref. [9].

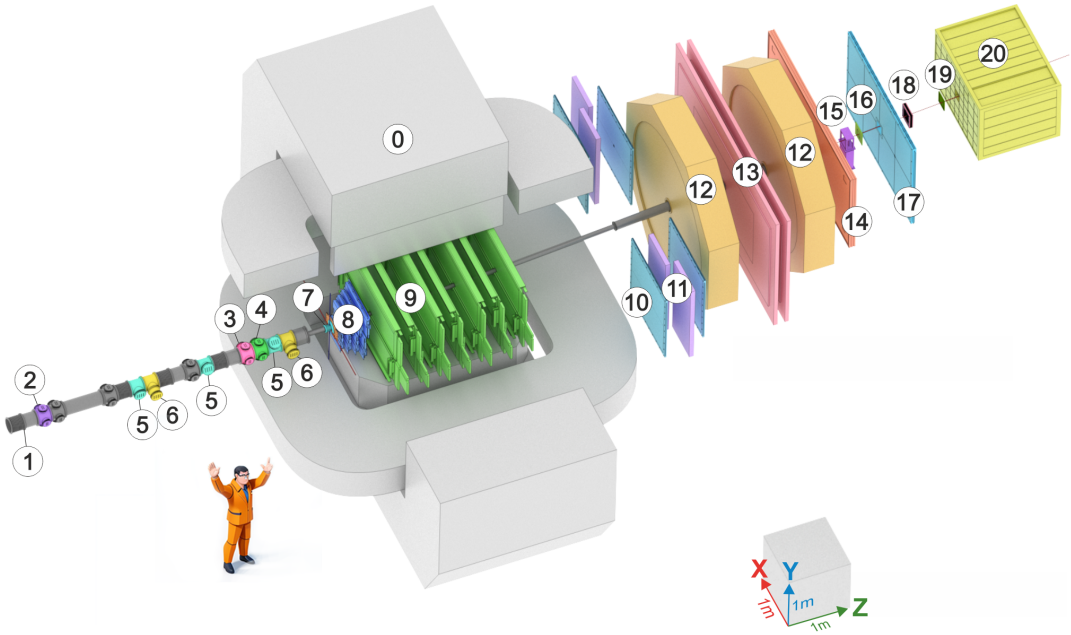

Figure 1: Three-dimensional view of the BM@N setup. 0) SP-41 analyzing magnet. 1) Vacuum beam pipe. 2) BC1 beam counter. 3) Veto counter. 4) BC2 beam counter. 5) Silicon Beam Tracker. 6) Silicon beam profilometers. 7) Barrel Detector. 8) Forward Silicon Detector. 9) Gaseous Electron Multiplier (GEM) detectors. 10) Small cathode strip chambers. 11) TOF400 system. 12) Drift chambers. 13) TOF700 system. 14) Scintillation Wall. 15) Fragment Detector. 16) Small GEM detector. 17) Large cathode strip chamber. 18) Gas ionization chamber as beam profilometer. 19) Forward Quartz Hodoscope. 20) Forward Hadron Calorimeter. The ion beam comes from the left through the vacuum beam pipe to avoid interactions with the air. Target is located inside the Barrel Detector (7).

3 Event reconstruction

For track reconstruction, a so-called Vector Finder toolkit [10, 11], implemented within the BmnRoot software framework [12], is used. It realizes a constrained combinatorial search for combinations of detector hits which can be potentially produced by the same particle. Track candidates found are fitted with a Kalman filter procedure.

The reconstructed tracks are used to find the primary (interaction) vertex. The vertex-fitting procedure is based on the Kalman filtering technique [13]. A similar Kalman-based approach is used in the decay reconstruction package, i.e. to find secondary (decay) vertices [14, 15].

Strange particles can be reconstructed from their weak decays to charged particles in the final state. Such decays create quite clear event topologies, as can be seen in Fig. 2, where a schematic view of one of such topologies, namely, a two-prong decay of a neutral particle (so-called “V0-decay”), is shown in the bending plane of the magnet, i.e. in the plane perpendicular to the magnetic field.

Such topologies can be identified using the secondary vertex reconstruction technique, which is based on selecting track combinations producing secondary (decay) vertices decoupled from the primary one (interaction point). The selection strength is controlled by applying different criteria on relevant kinematic and topological variables. For example, track combinations are accepted only if the

distance of the closest approach dca_{V0} in space between daughter tracks is smaller than some upper cut value. This cut ensures that the tracks originate from the same mother particle. To select decays of relatively long-lived particles, it is commonly required that the secondary vertex position is located farther than some lower cut distance $path$ from the primary one. In order to suppress the combinatorial background produced by primary tracks, the minimum value of the daughter track impact parameters to the primary vertex $dca_{p,\pi}$ should exceed some threshold. The quality of the decay reconstruction can be further improved by requiring the impact parameter of the decayed particle with respect to the primary vertex or its pointing angle, defined as the angle between its momentum and the direction vector from the primary to the secondary vertex, to be smaller than some value. The *DCA*-cuts can be also used normalized to their errors, i.e. expressed as their respective χ^2-values. In this way, it is possible to take into account the *DCA*-dependence on the transverse momentum, for example, and, therefore, to increase the selection power. In addition, to reject some fake tracks it was found to be quite useful to apply a track quality evaluation approach based on machine learning and implemented in the ROOT TMVA package. The classification based on the TMVA variable was used for 4- and 5-hit tracks.

For selected particle combinations, the invariant mass is calculated under the corresponding daughter particle hypotheses. Since, for this study, particle identification based on the TOF system is not used, the daughter particles are assumed to be a proton and a negative pion for the case of Λ hyperon and negative and positive pions for K^0_S meson reconstruction. Observation of clear peaks in the invariant mass distributions at the right particle mass values serves as a clear signature of the strange particle decays under study.

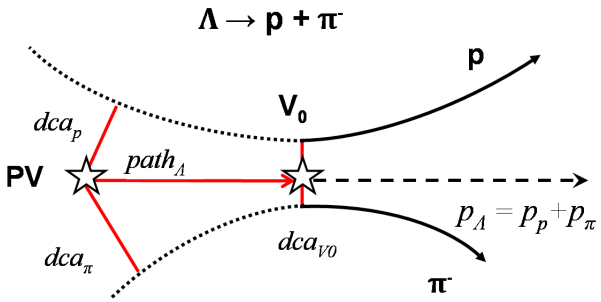

Figure 2: View of the Λ hyperon decay topology ($\rightarrow p+\pi^-$) in the bending plane of the magnetic field. Here, dca_p and dca_π are the distances of the closest approach (DCA) of the decay tracks to the primary vertex PV; dca_{V0} is the distance between daughter tracks in the mother decay vertex V_0; $path$ is the mother particle decay length, and $\mathbf{p}_p$, $\mathbf{p}_\pi$ and $\mathbf{p}_\Lambda$ are momenta of particles.

4 Λ hyperon and K^0_S meson reconstruction results

Figure 3 shows invariant mass distributions of Λ and K^0_S candidates after applying selection criteria, explained in the previous section. The exact values of the cuts are presented in Table 1. They were found from a multidimensional scan over parameter values. For each set of values the peak significance was calculated and the final result corresponds to its maximum. The significance is defined as $S/\sqrt{S+B}$, where S and B are the signal and background contributions inside some interval around the peak position, i.e. $S+B$ is the full integral of the invariant mass distribution over the interval width and S is the integral value after the background subtraction. The background contribution in the peak region can be estimated using either the polynomial fit outside it or the event mixing technique [16].

Having selected strange particle signal, the next step to proceed is to extract physics observables useful for comparison with other experiments and theoretical models. For this, first of all, it is necessary to check the consistency of selection cuts in experimental and simulated data. It can be done by looking at the particle yield versus one of the selection variables while keeping the others at their nominal value. As can be seen in Figs. 4, 5, the experimental and simulated results agree quite well, the residual difference is not essential for this study and can be taken into account in future analyses. Then the experimentally measured distributions should be corrected for the total detector efficiency. It is estimated from detector simulation and combines geometric efficiency (acceptance), efficiency of the tracking detectors and reconstruction efficiency. The validity of the efficiency estimates can be checked from some inclusive distributions (e.g., number of hits per reconstructed track), or from a reference (model - independent) process if possible. For strange particles under study, such a process is their weak decay. The obtained results on the lifetime measurement of Λ hyperons and K^0_S mesons are presented below along with some additional very preliminary results on strange particle production properties in Xe+CsI interactions, which better illustrate the reconstruction performance and should be considered as some validation steps toward physics analyses. The results presented were obtained for 5 million recorded triggers and 2 million Monte Carlo simulated events. This event statistics defines the errors shown in all the plots below. No systematic effects have been estimated at this stage.

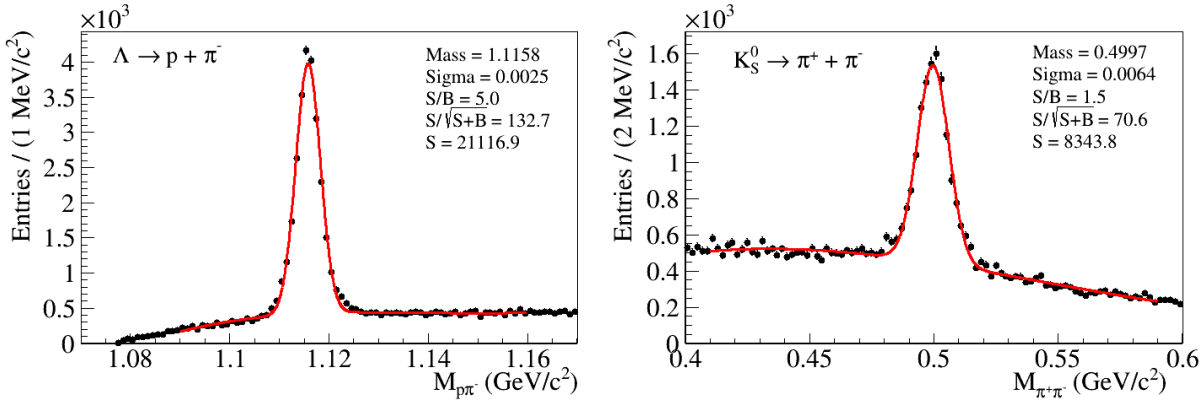

Figure 3: Invariant mass distributions of Λ (left) and K^0_S (right) candidates for 1 million collected events. The histograms are fitted by a sum of a gaussian and a 3-rd degree polynomial functions. The gaussian function is used to define the signal interval as $\pm 2.5\sigma$ around the peak position, while the polynomial function is used to evaluate the background under the peak. The numbers in the legend show the peak position and σ of the gaussian function, signal-to-background ratio, significance and signal contribution inside the signal interval.

4.1 Λ hyperon

To illustrate the efficiency effect on the decay curve, Fig. 6 shows the decay time (lifetime) distribution of all Λ hyperons produced by the Monte Carlo event generator DCM-SMM [17] and the ones after detector simulation, event reconstruction and decay selection procedures presented above. The distortion is quite visible. The lifetime t in the particle's rest frame is calculated according to the formula

$$t = L \cdot m_0/(p \cdot c), \tag{1}$$

Table 1: Selection criteria used for Λ and K^0_S reconstruction. Cuts on DCAs are imposed in the χ^2-space, i.e., after normalization to respective parameter errors.

Cut	Λ	K^0_S
DCA of daughters to primary vertex	$> 6.3(\pi), > 5.3(p)$	$> 6.8(\pi^-), > 10.8(\pi^+)$
DCA of mother to primary vertex	<4.5	<4.4
Decay length, cm	>2.0	>1.0
TMVA	$> -0.03(\pi), > -0.03(p)$	$> 0.0(\pi^-), > -0.08(\pi^+)$

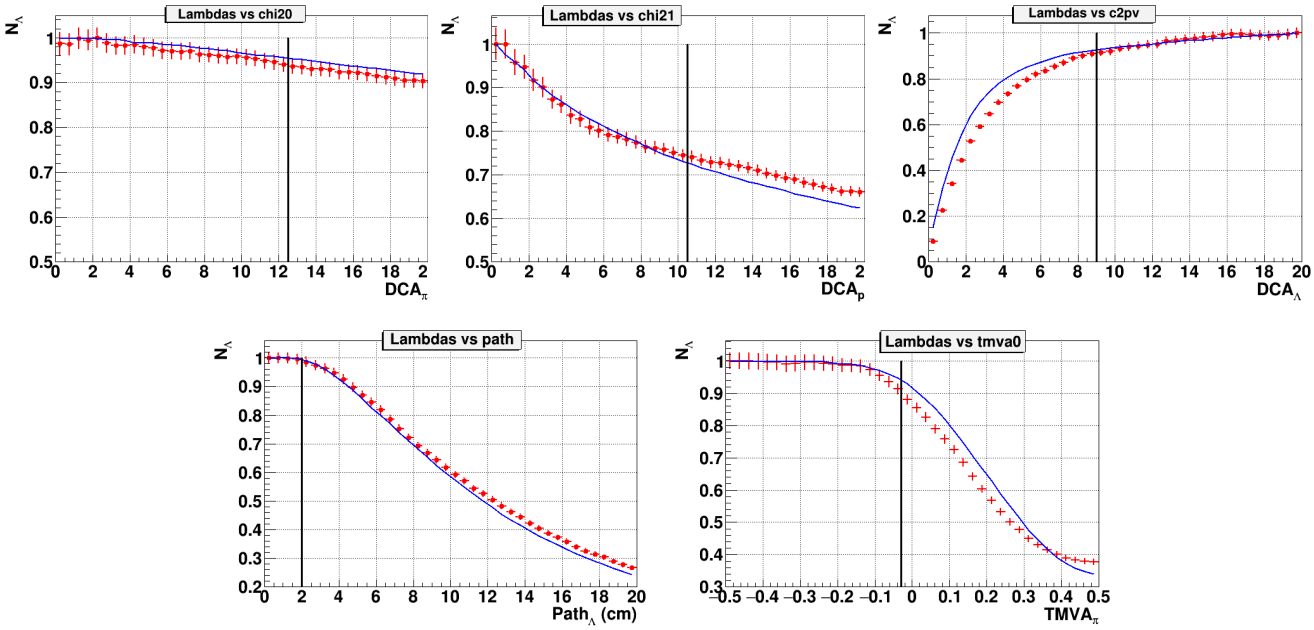

Figure 4: Λ hyperon reconstructed yield versus different selection cuts. The other variables are set to their nominal values (see Table 1 and vertical lines on the plots). Histograms are normalized to their values at the maximum. Red symbols represent experimental data, blue lines simulated ones.

where L is the decay length, m_0 and p are the mass and momentum of the particle and c is the speed of light. The decay time distribution is described by the formula

$$dN/dt = N_0/\tau \cdot \exp(-t/\tau), \tag{2}$$

where N_0 is the total number of particles and τ is the mean lifetime. The original decay curve can be reconstructed from measurements in several lifetime intervals (e.g., in 9 lifetime bins, shown on the right plot of Fig. 6). Figures 7 and 8 illustrate the sequence of the steps of the decay curve reconstruction procedure which consists in the following. Λ hyperon invariant mass distribution is built for each lifetime interval (Fig. 7left). After background subtraction (Fig. 7right), the yield is calculated as the number of counts in the peak region, i.e. within $\pm 2.5\sigma$ around the invariant mass peak maximum position. This means that the gaussian peak fit is used only to define the signal region and not to extract the particle yield, since the gaussian fit does not take into account possible distortion of the peak shape. These sums of histogram counts give the raw (uncorrected) lifetime distribution (Fig. 8left). The statistical errors shown are calculated as

$$\Delta S = \sqrt{T + B}, \tag{3}$$

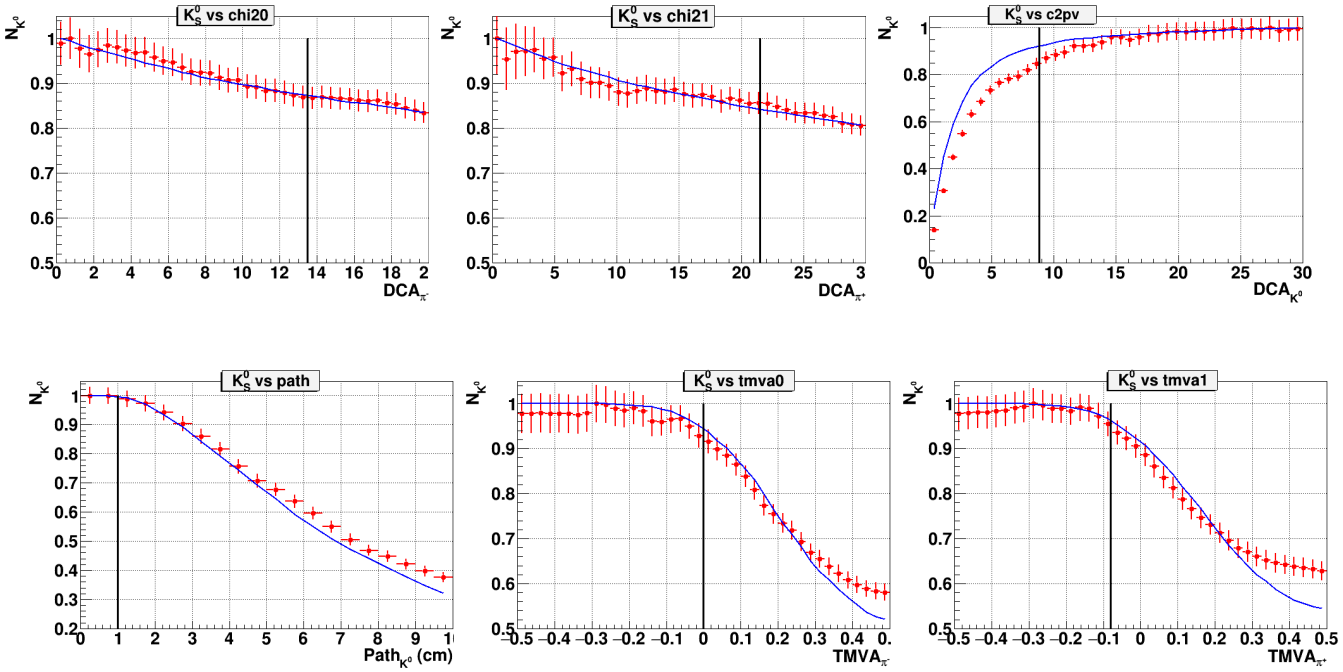

Figure 5: K^0_S meson reconstructed yield versus different selection cuts. The other variables are set to their nominal values (see Table 1 and vertical lines on the plots). Histograms are normalized to their values at the maximum. Red symbols represent experimental data, blue lines simulated ones.

where ΔS is the extracted signal error, T is the total histogram counts (before background subtraction) in the peak region and B is the background estimate. The total reconstruction efficiency is estimated from the Monte Carlo simulation (Fig. 8right) and defined as a ratio of fully reconstructed hyperons after final selection cuts to the ones produced in the full phasespace (and within 30 cm from the interaction point to reject hyperons created in the detector material). The efficiency is used to correct the raw distribution and extract the original one (Fig. 8bottom).

Transverse momentum spectra of particles provide important information about physics processes during nucleus - nucleus interactions. For practical purposes, the transverse momentum p_T is often substituted by the transverse mass $m_T \equiv \sqrt{(p_T^2 + m_0^2)}$, where m_0 is the particle mass. Transverse mass spectra can be obtained following the procedure similar to the one described above, i.e. obtaining particle yields from background-subtracted invariant mass spectra in bins of m_T and correcting for reconstruction efficiency. Validity of the efficiency estimates can be verified again from the reconstructed decay curve obtained from hyperon yields in lifetime intervals, where the yields are found from the corrected for efficiency m_T spectra for those lifetime bins. Thus, the procedure is based on a double - differential analysis, i.e. invariant mass distributions similar to Fig. 7 are constructed for two - dimensional $m_T - t$ bins. Then the raw m_T spectra (Fig. 9left) are corrected for the efficiency (Fig. 9right) defined as in the previous case but for the intervals of the lifetime. The corrected scaled m_T spectra, i.e. $1/m_T^2 \cdot dN/dm_T$, are fitted to the Boltzman expression [18]:

$$\frac{1}{m_T^2}\frac{dN}{dm_T} = C(t) \cdot \exp\left(-\frac{m_T - m_0}{T_{eff}}\right), \tag{4}$$

where $C(t)$ is the normalization constant and T_{eff} is the so-called effective temperature (which is the inverse slope parameter of the exponential distribution). The fitting functions (Fig. 10left and right) are used to integrate dN/dm_T spectra and to obtain hyperon yields for the lifetime intervals

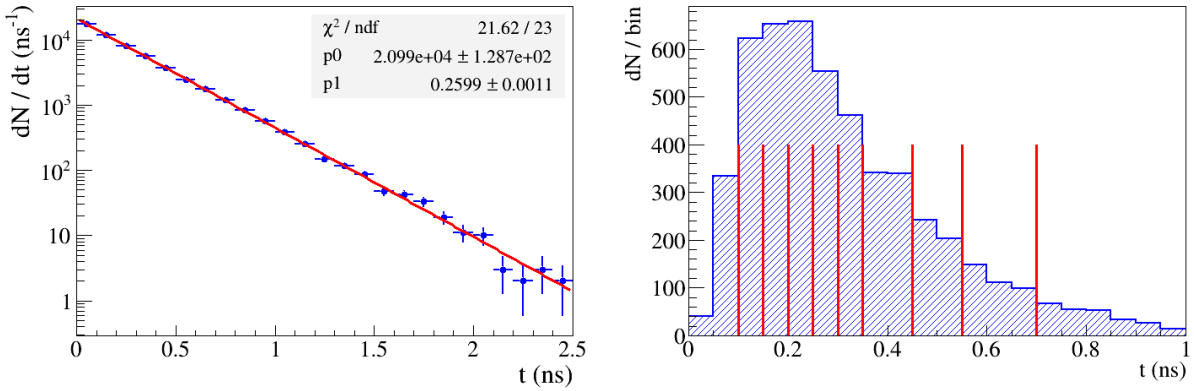

Figure 6: (Left) lifetime distribution of all generated Λ hyperons fitted to the decay curve given by formula (2) with $p1$ being the mean lifetime τ (the table value of 0.263±0.002 ns). (Right) lifetime distribution after detector simulation, event reconstruction and decay selection procedures. Vertical lines represent time intervals which were used to reconstruct the decay curve.

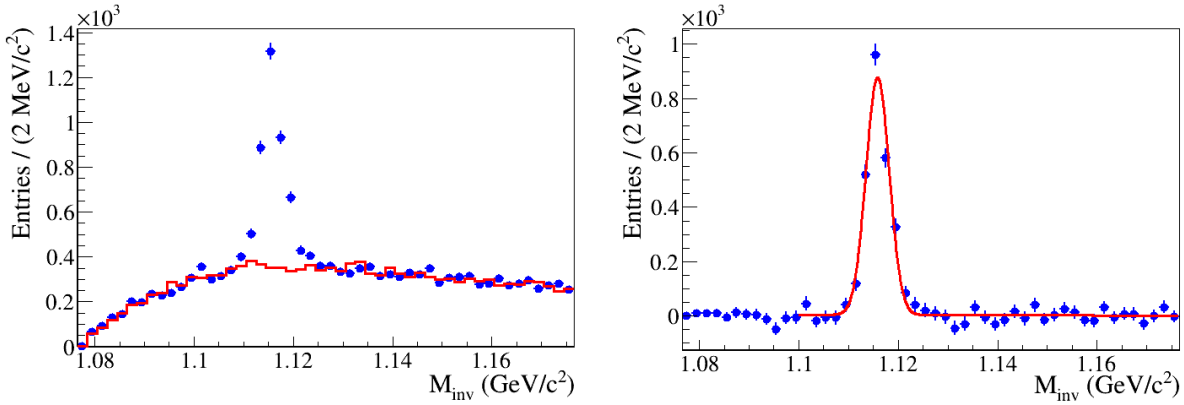

Figure 7: Invariant mass distributions of Λ candidates for the decay time bin of 0.1 - 0.2 ns before (left) and after (right) background subtraction.

(Fig. 10bottom). The integration over m_T is done as follows:

$$N(t) = \int_0^\infty \frac{dN}{dm_T} dm_T = C(t) \int_0^\infty m_T^2 \cdot \exp\left(-\frac{m_T - m_0}{T_{eff}}\right) dm_T = C(t) \cdot \left(2T_{eff}^3 + 2T_{eff}^2 m_0 + T_{eff} m_0^2\right). \quad (5)$$

The resulting lifetime distribution is well fitted to the decay curve with a reasonable value of the mean lifetime. The obtained values of T_{eff} for different lifetime bins are close to each other as can be expected from the fact, that particle lifetime is not a variable which selects a particular region of the phasespace characterized by the effective temperature.

The next step toward physics analyses is reconstruction of particle m_T spectra in different rapidity y intervals. This can be done by extracting particle yields in 2-dimensional bins of $m_T - y$ and correcting for the total efficiency similar to the procedure described above. Results are illustrated in Figs. 11, 12 for 4 intervals of the proton-proton centre-of-mass rapidity $y_{cm} = y - 1.17$. Figure 12 shows the Λ hyperon rapidity spectrum dN/dy fitted to the gaussian function with zero mean value. The spectrum was produced for events where a primary vertex was reconstructed with at least two

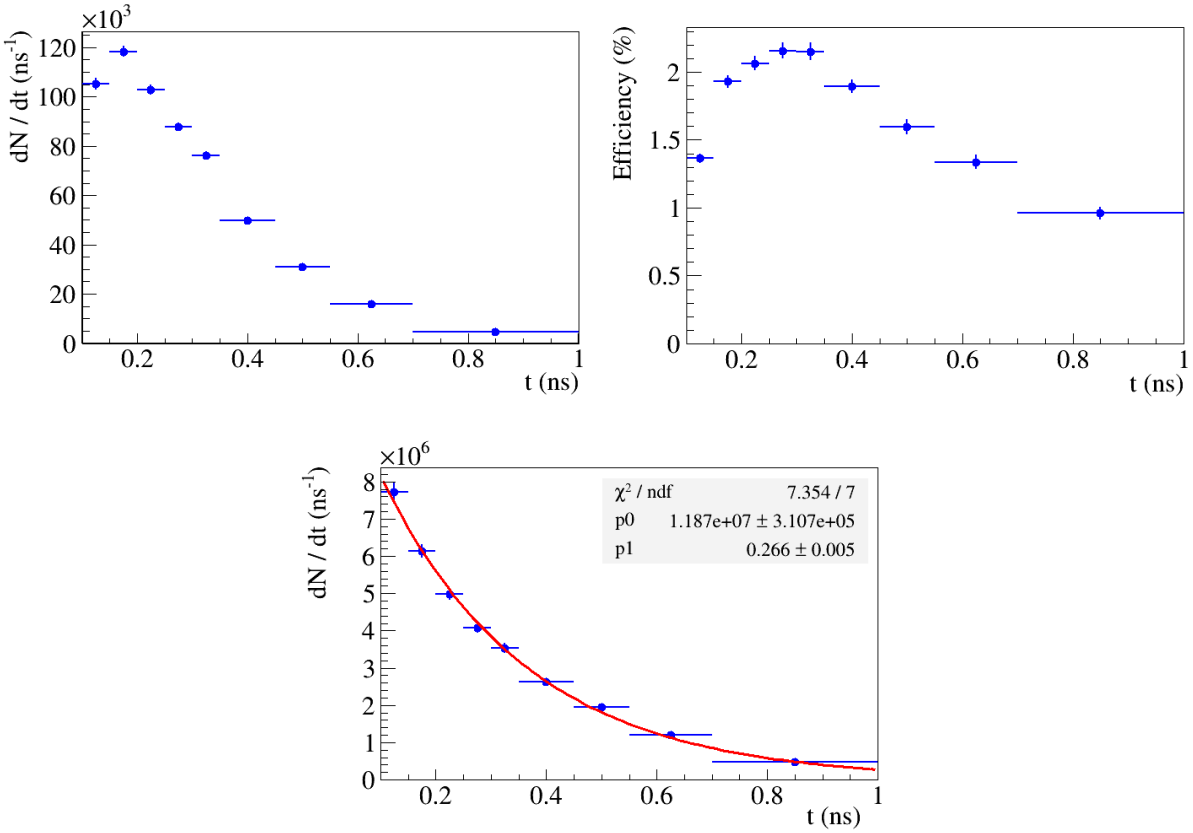

Figure 8: (Left) reconstructed Λ hyperon yield versus lifetime; (right) total Λ hyperon efficiency obtained from Monte Carlo simulation; (bottom) Λ hyperon lifetime distribution corrected for efficiency, fitted to the decay curve (2).

tracks, From the Boltzman fits one can see obvious rapidity dependence of the effective temperature T_{eff} and the trend is similar to previously observed in nuclear collisions [18].

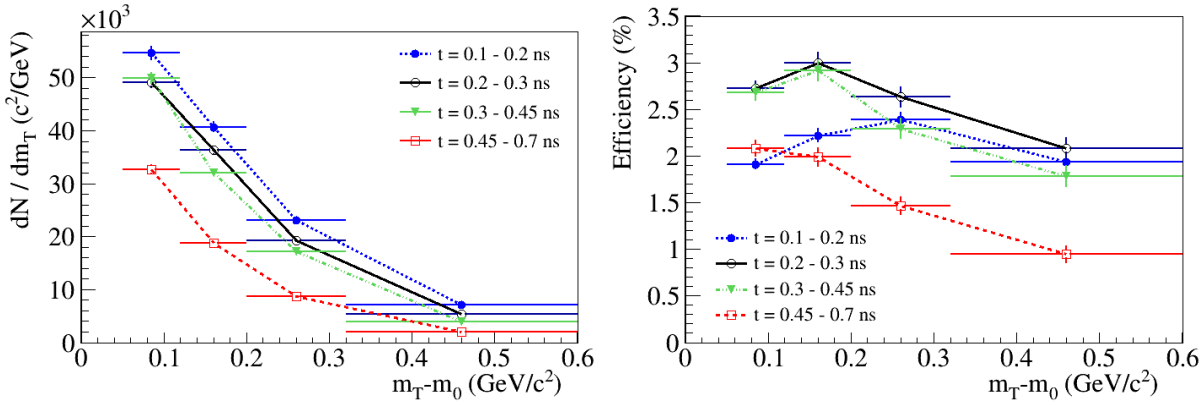

Figure 9: (Left) Λ hyperon raw yields versus transverse mass for 4 intervals of lifetime; (right) total reconstruction efficiency versus m_T for 4 lifetime intervals. Lines are drawn to guide the eye.

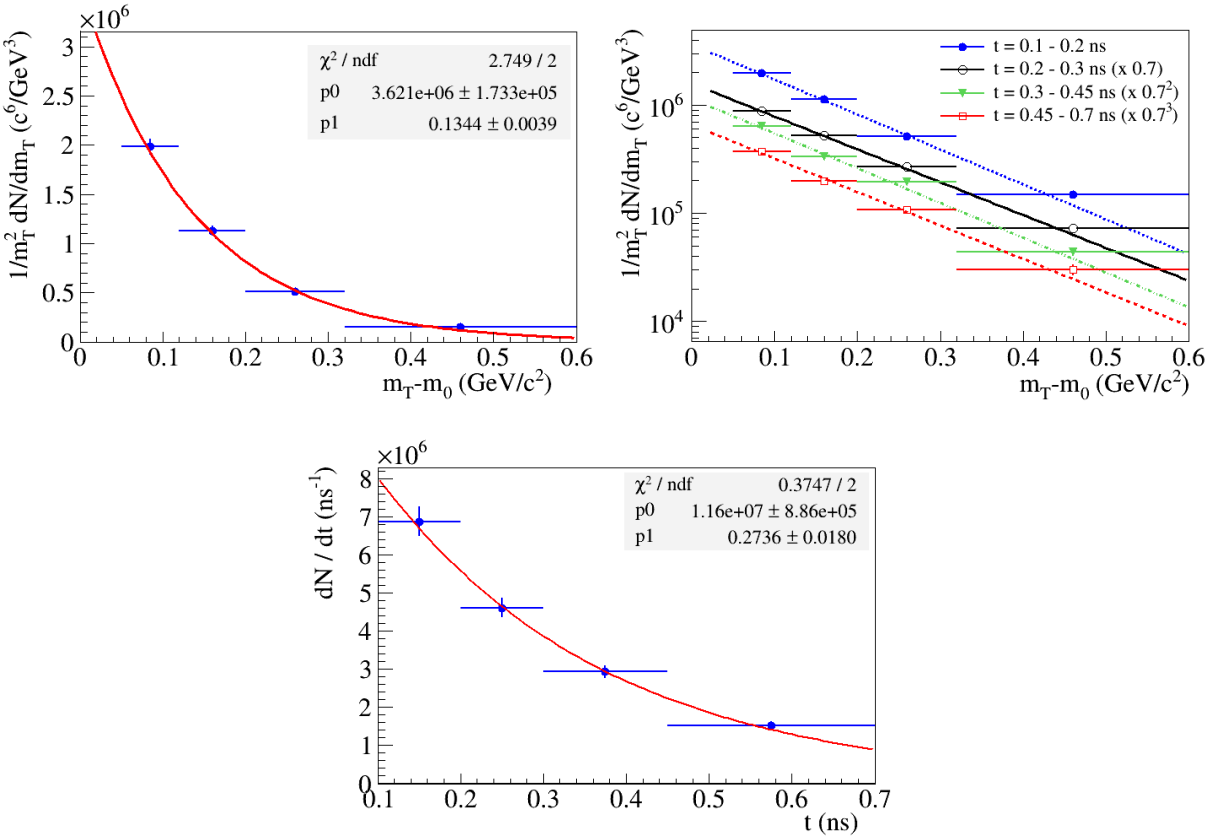

Figure 10: (Left) corrected for efficiency transverse mass distribution of Λ hyperons for the lifetime bin of 0.1 - 0.2 ns fitted to the Boltzman expression (4); (right) the same for 4 lifetime bins. The effective temperatures T_{eff} obtained are: 134±4, 143±4, 135±4 and 140±7 MeV for the lifetime bins of 0.1 - 0.2, 0.2 - 0.3, 0.3 - 0.45 and 0.45 - 0.7 ns, respectively. (Bottom) reconstructed decay curve from integrated m_T spectra fitted to the expression (2).

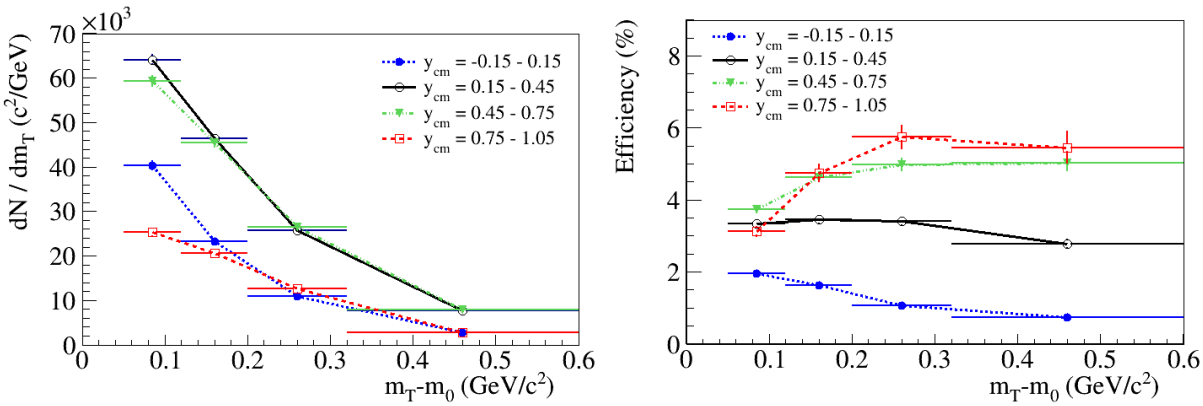

Figure 11: (Left) Λ hyperon raw yields versus transverse mass for 4 intervals of rapidity; (right) total reconstruction efficiency versus m_T for 4 rapidity intervals. Lines are drawn to guide the eye.

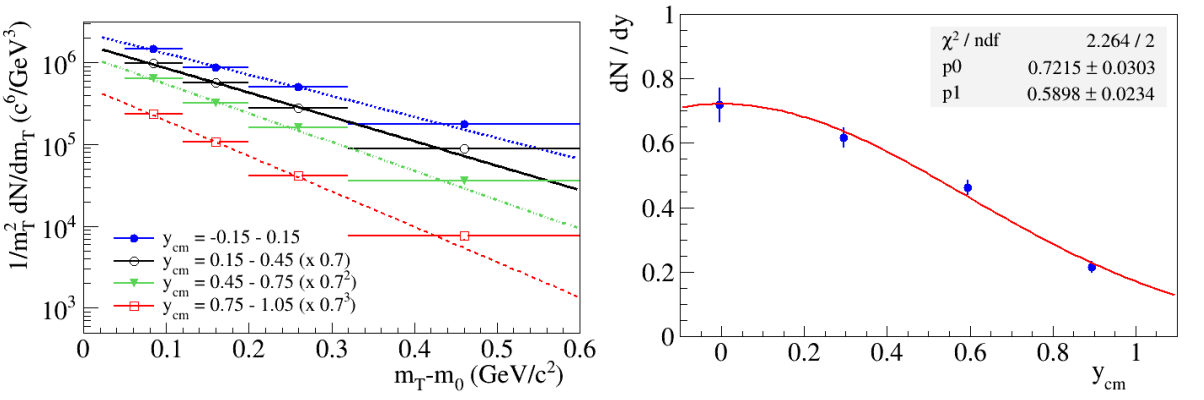

Figure 12: (Left) transverse mass distributions of Λ hyperons for 4 rapidity bins fitted to the Boltzman expression. The effective temperatures T_{eff} obtained are: 170±8, 144±4, 126±3 and 105±4 MeV with the highest value corresponding to the lowest rapidity interval. (Right) Λ hyperon rapidity spectrum fitted to the gaussian with zero mean (full line).

4.2 K^0_S meson

The same procedure was applied to reconstruct K^0_S decays. The obtained results are presented in Figs. 13 - 17.

Figure 13 illustrates the steps to reconstruct the decay curve from the raw lifetime distribution and the estimated total reconstruction efficiency. Figures 14 and 15 show how the efficiency - corrected m_T spectra are built and used to obtain the decay curve after proper integration, while Figs. 16 and 17 demonstrate the steps to reconstruct the rapidity spectrum. From Figs. 17 and 12 one can estimate the approximate yield ratio of Λ hyperons and K^0_S mesons. The obtained value of $\sim$3.5 at zero rapidity qualitatively agrees with the ratio measured at the STAR experiment in Au+Au fixed-target run at the beam kinetic energy of 2.91A GeV ($\sqrt{s_{NN}}$ = 3 GeV) [19], confirming the baryon - dominated nature of the nuclear matter at such collision energies.

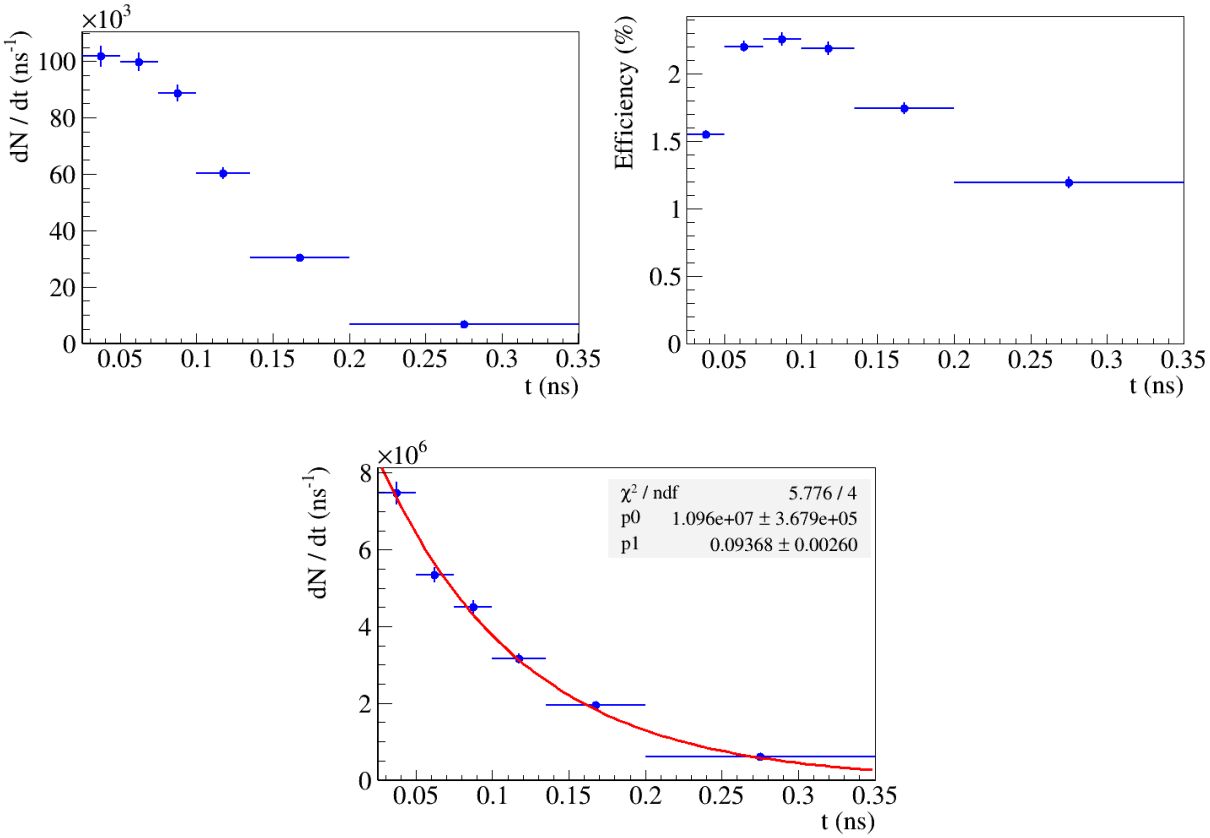

Figure 13: (Left) reconstructed K^0_S meson yield versus lifetime; (right) total K^0_S meson efficiency obtained from Monte Carlo simulation; (bottom) K^0_S meson lifetime distribution corrected for efficiency, fitted to the decay curve (2) with $p1$ table value of 0.090 ns.

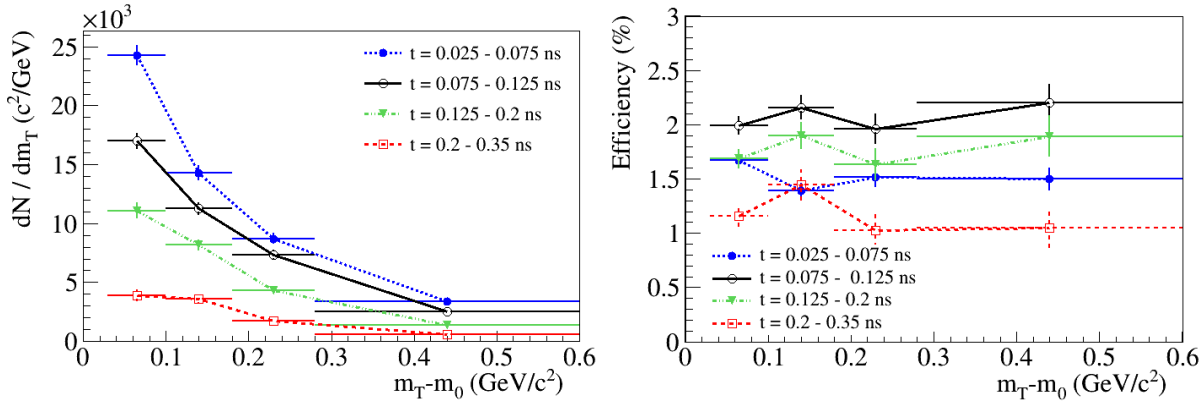

Figure 14: (Left) K^0_S meson raw yields versus transverse mass for 4 intervals of lifetime; (right) total reconstruction efficiency. Lines are drawn to guide the eye.

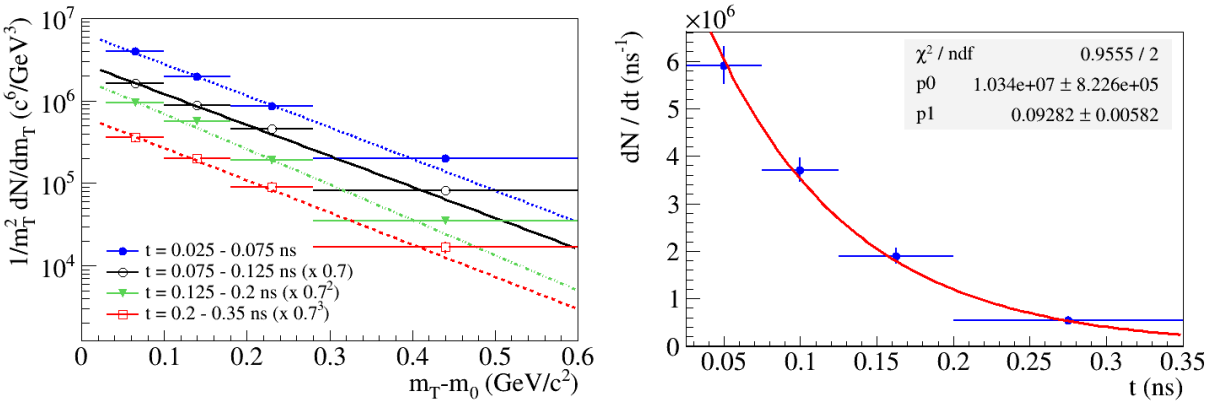

Figure 15: (Left) transverse mass distributions of K^0_S mesons for 4 lifetime bins fitted to the Boltzman expression (4). The effective temperatures T_{eff} obtained are: 113±3, 116±3, 101±4 and 111±8 MeV for the lifetime bins of 0.025 - 0.075, 0.075 - 0.125, 0.125 - 0.2 and 0.2 - 0.35 ns, respectively. (Right) reconstructed decay curve from integrated m_T spectra fitted to the expression (2).

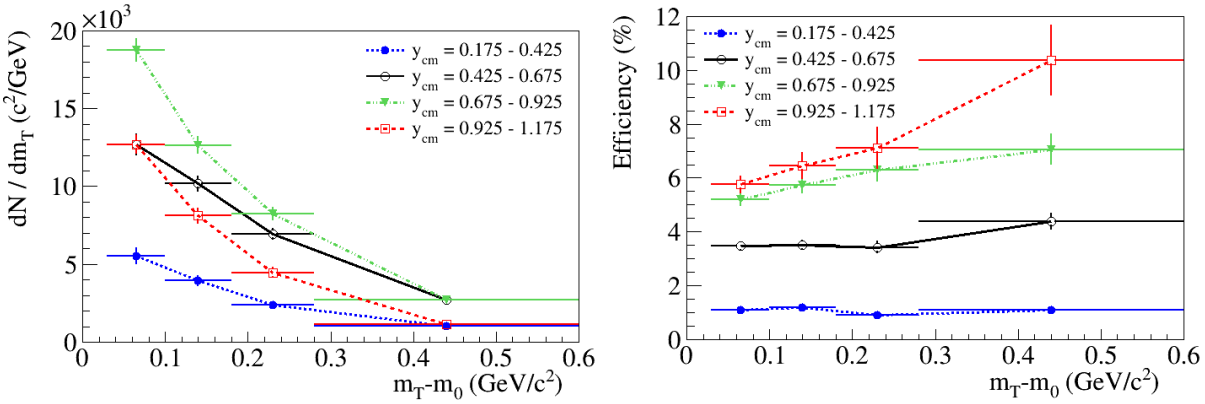

Figure 16: (Left) K^0_S meson raw yields versus transverse mass for 4 intervals of rapidity; (right) total reconstruction efficiency. Lines are drawn to guide the eye.

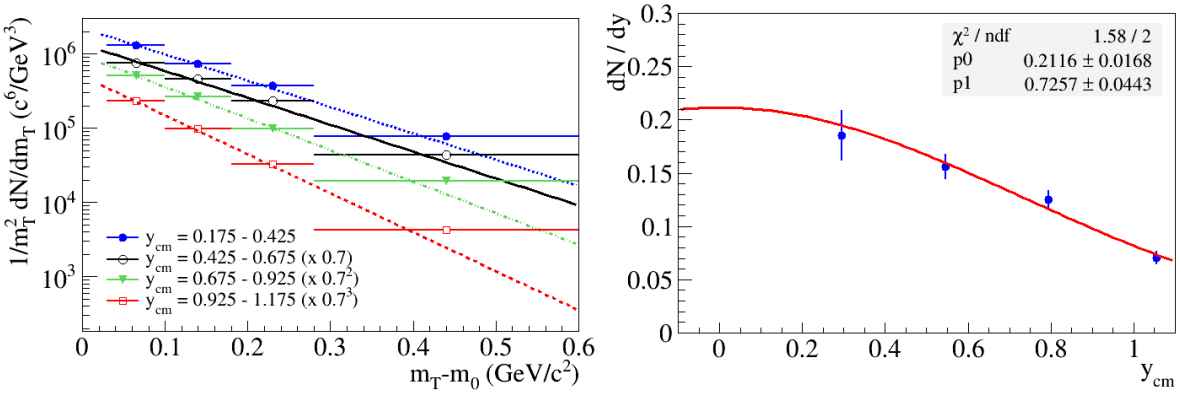

Figure 17: (Left) Transverse mass distributions of K^0_S mesons for 4 rapidity bins fitted to the Boltzman expression (4). The effective temperatures T_{eff} obtained are: 122±7, 120±4, 102±3 and 83±3 MeV with the highest value corresponding to the lowest rapidity interval. (Right) K^0_S meson rapidity spectrum fitted to the gaussian with zero mean value (full line).

5 Study of Λ hyperon production

5.1 Data set

During data taking period of the run 8 the running conditions were changing as can be seen in Fig. 18, where the raw Λ yields (number of reconstructed Λ per event with a reconstructed primary vertex) are shown on the run-by-run basis. Primary vertex is defined as reconstructed if it is built from at least 2 tracks. As can be seen, yield variation is quite significant. Figure 18right presents the yield distribution. One can see 5 peaks in the distribution denoted by leters "A" though "E" with the group "A" runs showing the largest reconstructed yield, i.e. the best quality. The following analysis is based on event sets from the groups "A" through "C" containing 367 runs with statistics ∼220 million events with reconstructed primary vertex. The data sample obtained after applying selection criteria amounts to about 6.6 million Λ hyperons.

5.2 Tuning of the Monte Carlo simulation

To extract useful physics information, the raw yields obtained from the invariant mass distributions should be corrected for the reconstruction efficiency which can be determined from the Mont Carlo simulation. Varying running conditions require different Monte Carlo tuning for different subsets of events, e.g. for run groups "A" - "C". On the other hand, different event samples provide a possibility of the additional cross-check of the analysis, i.e. they allow validation of efficiency estimations.

Monte Carlo tuning can be qualitatively controlled by comparing distributions of the number of hits attached to daughter tracks in experimental and simulated data in different regions of the phasespace. To avoid possible biases, it is necessary to apply decay selection cuts and use mass window around the invariant mass peak position. An example of such distributions is presented in Figs. 19 - 21 for run groups "A" - "C".

Initial Monte Carlo tuning included hit-to-track residual adjustment for different tracking stations (applying MC hit smearing where necessary). Then, for each run group, detector efficiency corrections were applied, i.e. Monte Carlo hits were randomly killed in detector regions where the obtained MC efficiency estimations exceeded those in real data. The detector efficiency was defined in terms of the probability of a hit to be found in close proximity to the reconstructed track position in this detector. The size of the proximity region was varied in the dedicated tests. Somewhat different definitions of the efficiency were also tried. The best so far agreement of the simulated and experimental results in terms of the number of hits per track was achieved for the proximity region radius of 2 mm and shown in Figs. 19 - 21.

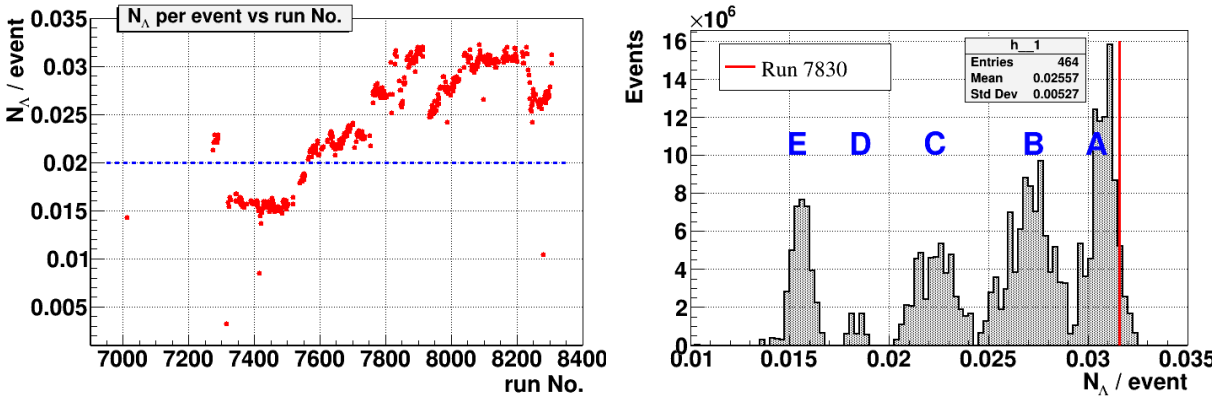

Figure 18: Raw Λ hyperon yield (number of reconstructed Λ per event with reconstructed primary vertex) versus run number (left) and the run-by-run distribution of the raw yield (right). Letters "A" through "E" denote run groups.

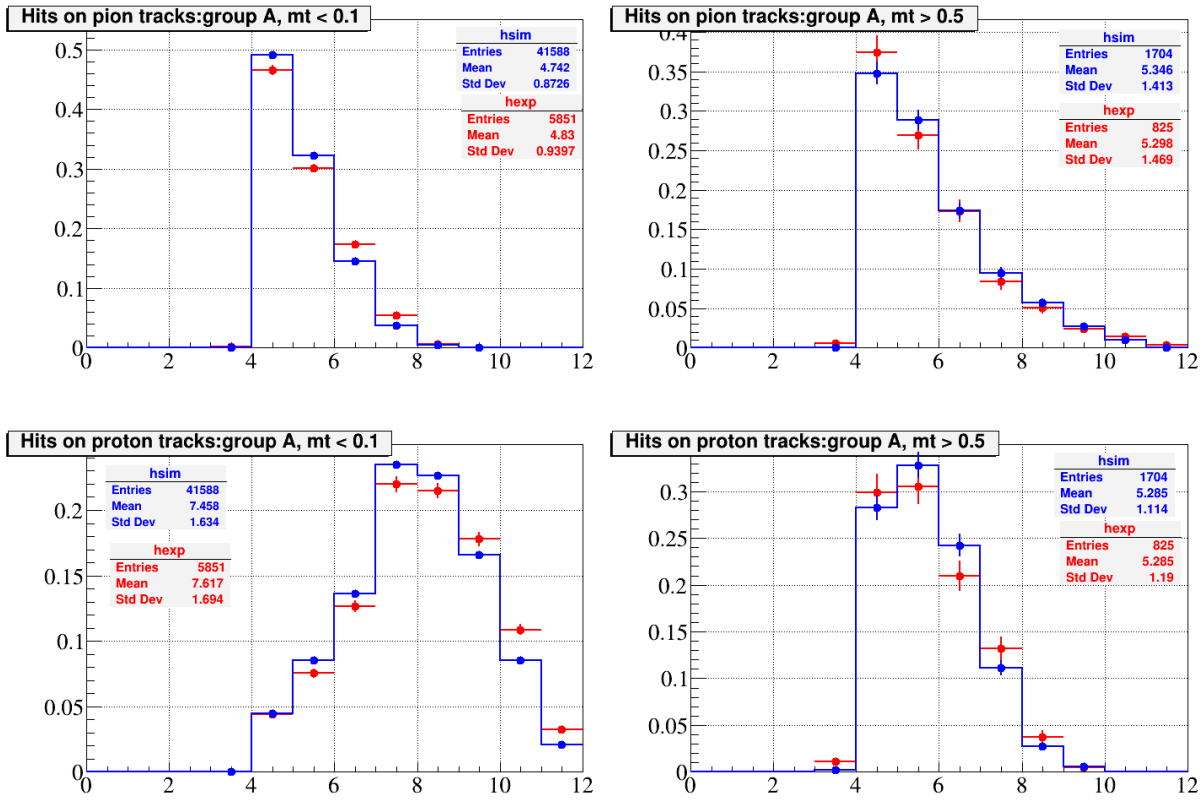

Figure 19: Distributions of the number of hits per track of Λ daughters for events from the group A: left column - $p\pi$ combinations with $m_T - m_0 < 0.1$ GeV/c^2, right column - $m_T - m_0 > 0.5$ GeV/c^2. Upper row - pions, lower row - protons; Markers present experimental data, lines - simulated data. Histograms are mormalized to the total number of entries. Results are shown for centrality interval 0-10% and Λ rapidity $-0.1 < y_{CMS} < 0.1$.

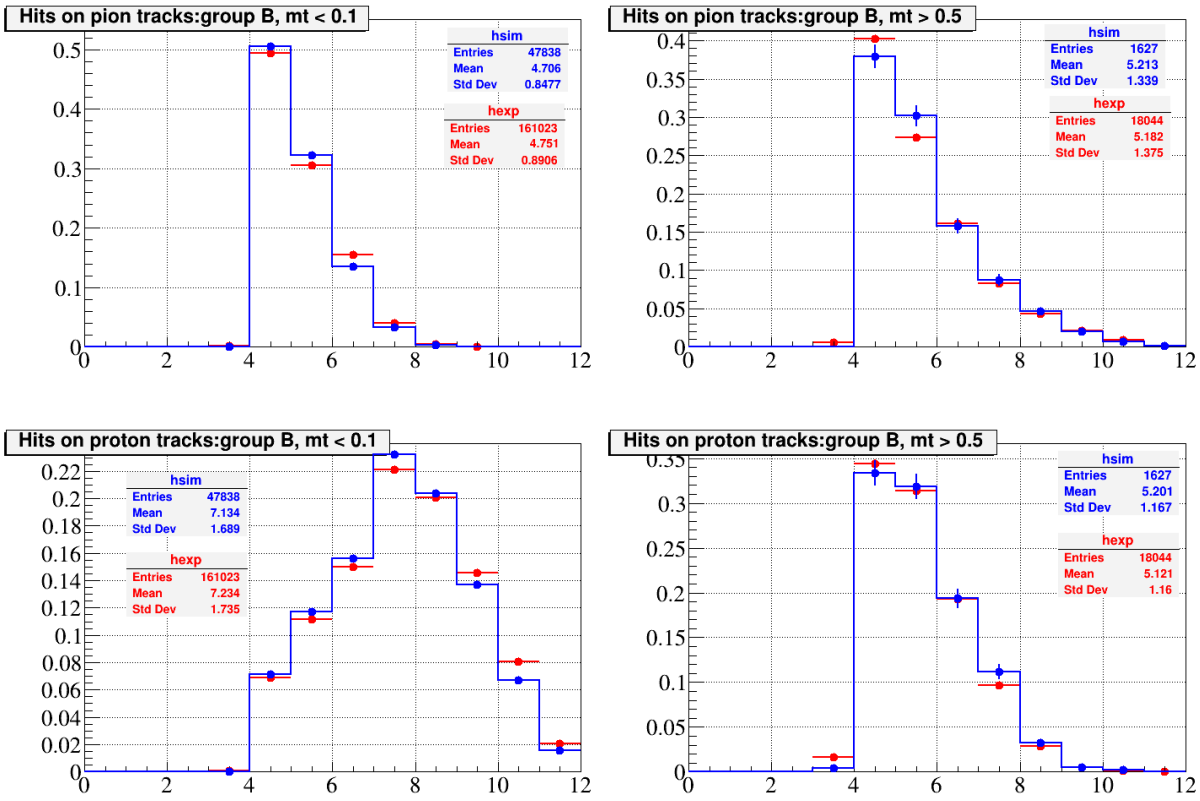

Figure 20: Distributions of the number of hits per track of Λ daughters for events from the group B.

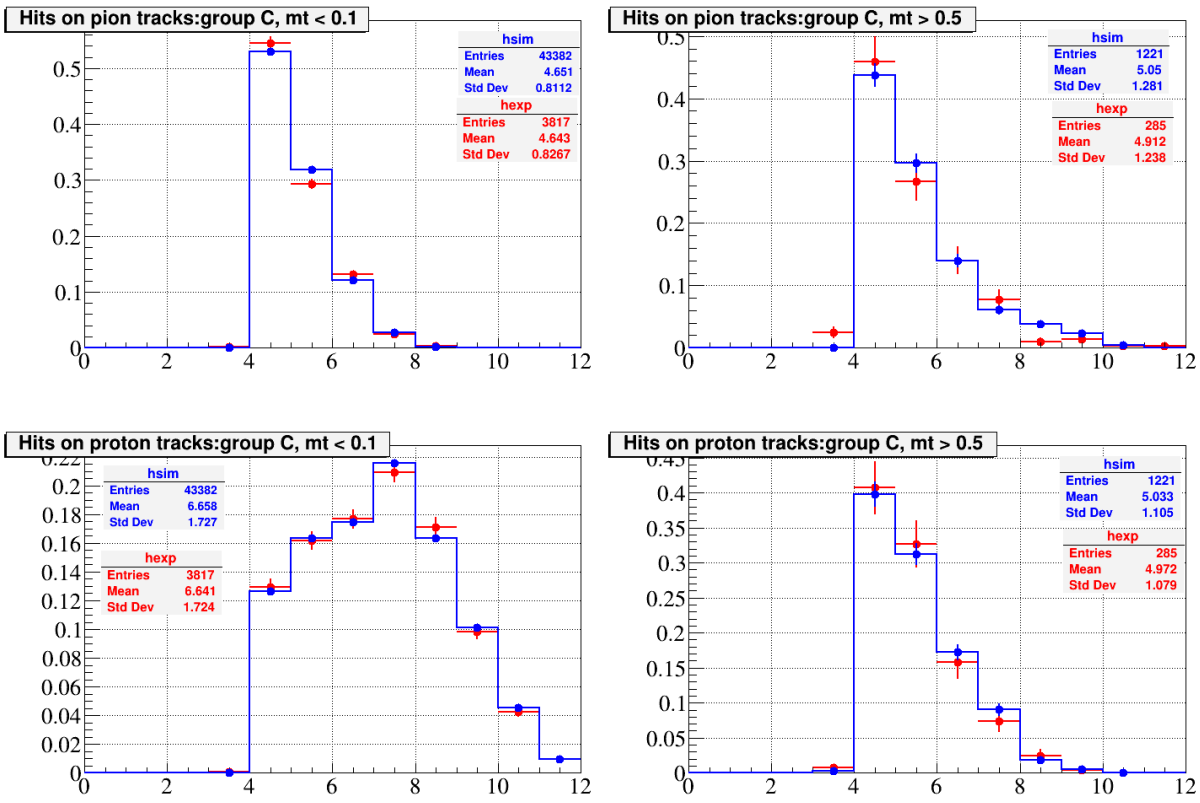

Figure 21: Distributions of the number of hits per track of Λ daughters for events from the group C.

5.3 Transverse mass spectra and dN/dy of Λ hyperons

Figures 22 - 27 present Λ hyperon transverse mass spectra for centrality bin 0-10% and 6 rapidity intervals. Shown are the spectra obtained for event sets from the groups A-C as well as the combined result, where the invariant mass spectra for the 3 samples were merged with the weights inversely proportional to their efficiencies.

The results on Λ rapidity density (dN_Λ/dy) obtained after proper integration according to Expr. 5 and effective temperature T_{eff} are presented in Fig. 28 as functions of rapidity in the centre-of-mass system (y_{CMS}). The plots also include current estimates of the systematic uncertainty. T_{eff} error amounts to 10% and evaluated from its variations in different approaches to detector efficiency determination. The error on dN/dy combines 5% uncertainty of the signal extraction procedure, 10% due to centrality and 10% due to detector efficency determination procedures.

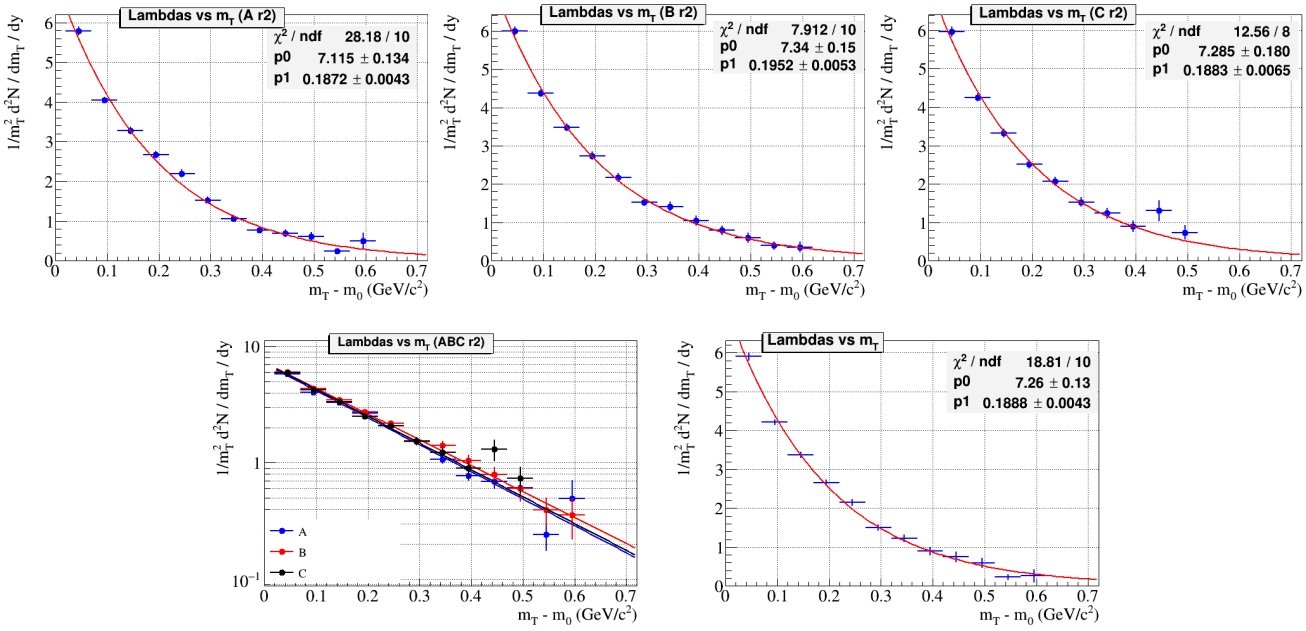

Figure 22: Λ hyperon transverse mass spectra. Upper row from left to right: event samples A, B, C. Lower left: A, B and C samples superimposed. Lower right: combined statistics. 0-10% collision centrality, $-0.3 < y_{CMS} < -0.1$.

6 Study of K^0_S meson production

Figures 29, 30 present K^0_S meson transverse mass spectra for centrality bin 0-10% and 6 rapidity intervals. Shown are the spectra obtained for event sets from the groups A-C as well as the combined result, where the invariant mass spectra for the 3 samples were merged with the weights inversely proportional to their efficiencies.

The results on K^0_S rapidity density (dN/dy) obtained after proper integration according to Expr. 5 and effective temperature T_{eff} are presented in Fig. 31 as functions of rapidity in the centre-of-mass system (y_{CMS}). The plots also include current estimates of the systematic uncertainty. T_{eff} error amounts to 10% and evaluated from its variations in different approaches to detector efficiency determination. The error on dN/dy combines 5% uncertainty of the signal extraction procedure, 10% due to centrality and 10% due to detector efficency determination procedures.

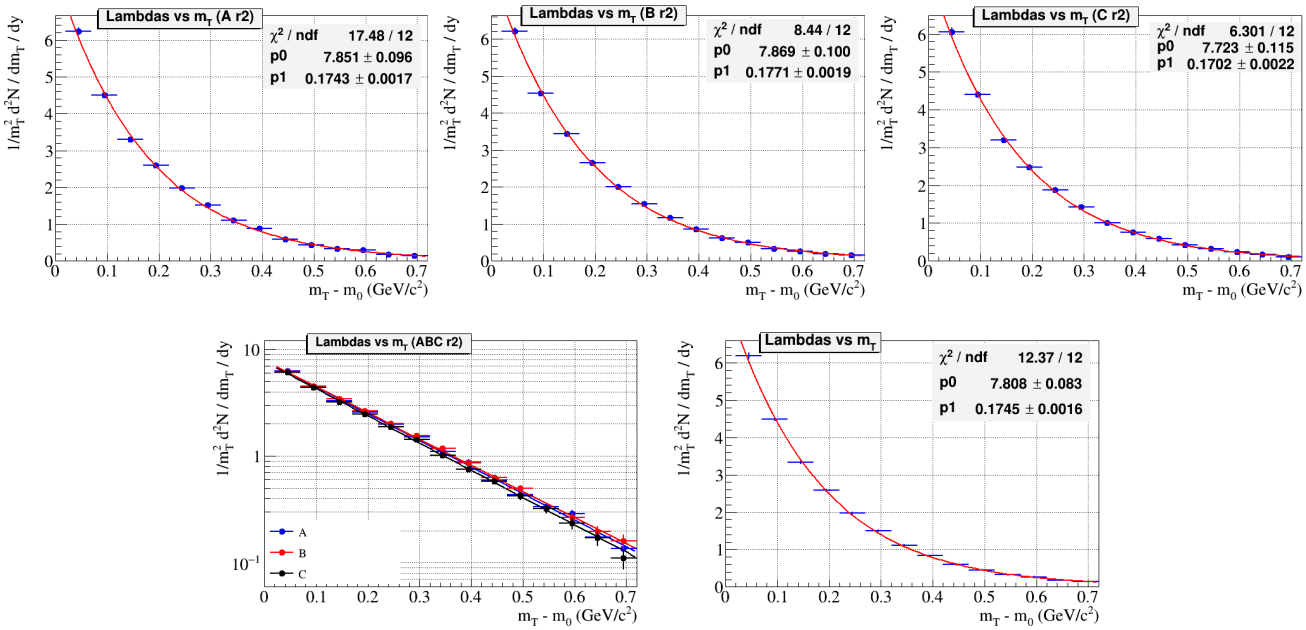

Figure 23: Λ hyperon transverse mass spectra. Upper row from left to right: event samples A, B, C. Lower left: A, B and C samples superimposed. Lower right: combined statistics. 0-10% collision centrality, $-0.1 < y_{CMS} < 0.1$.

7 Summary and future developments

The procedures for reconstruction of strange particle decays at the BM@N experiment have been described and their performance demonstrated. As a validation step of the developed and implemented reconstruction approach, some very preliminary results on strange particle production in Xe+CsI interactions at 3.8A GeV beam energy have been presented. The physics analysis further proceeded with a more detailed study of Λ hyperon and K^0_S meson production on large statistics The preliminary results on particle rapidity density dN/dy and effective temperature T_{eff} as functions of the centre-of-mass rapidity y_{CMS} have been obtained for collision centrality 0-10%. Main systematics effects have been evaluated as well.

Future steps include obtaining results on Λ and K^0_S production for different centrality classes as well as further analysis of the influence of the systematic effects on the results obtained.

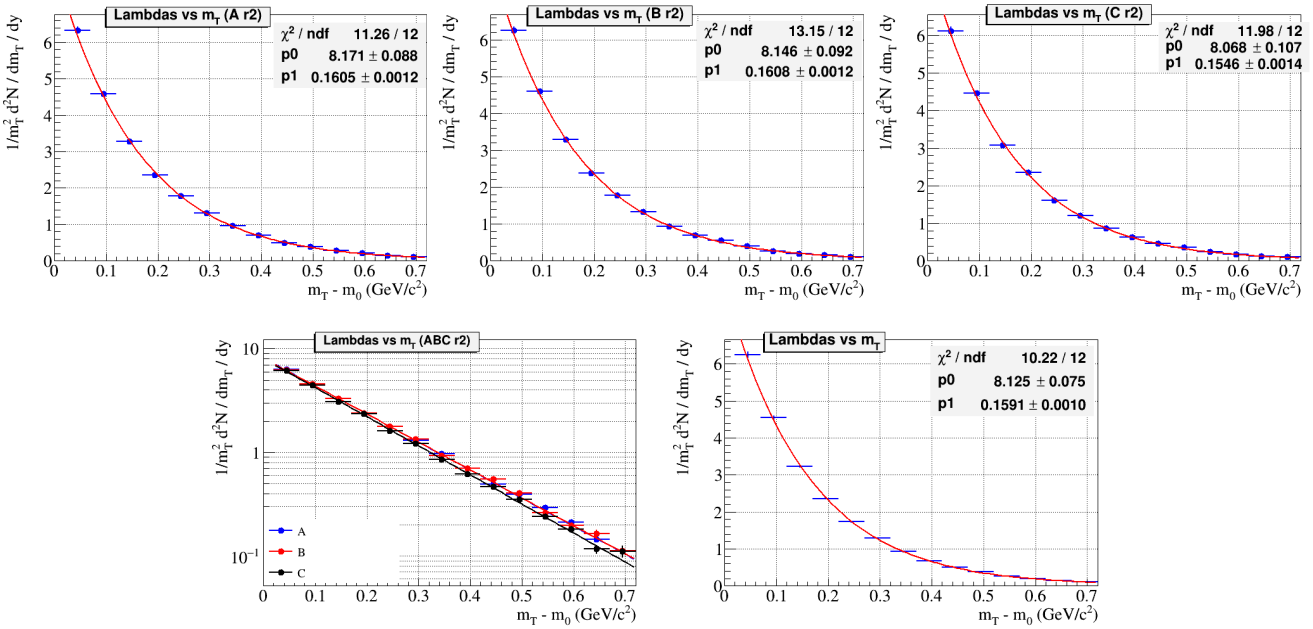

Figure 24: Λ hyperon transverse mass spectra. Upper row from left to right: event samples A, B, C. Lower left: A, B and C samples superimposed. Lower right: combined statistics. 0-10% collision centrality, $0.1 < y_{CMS} < 0.3$.

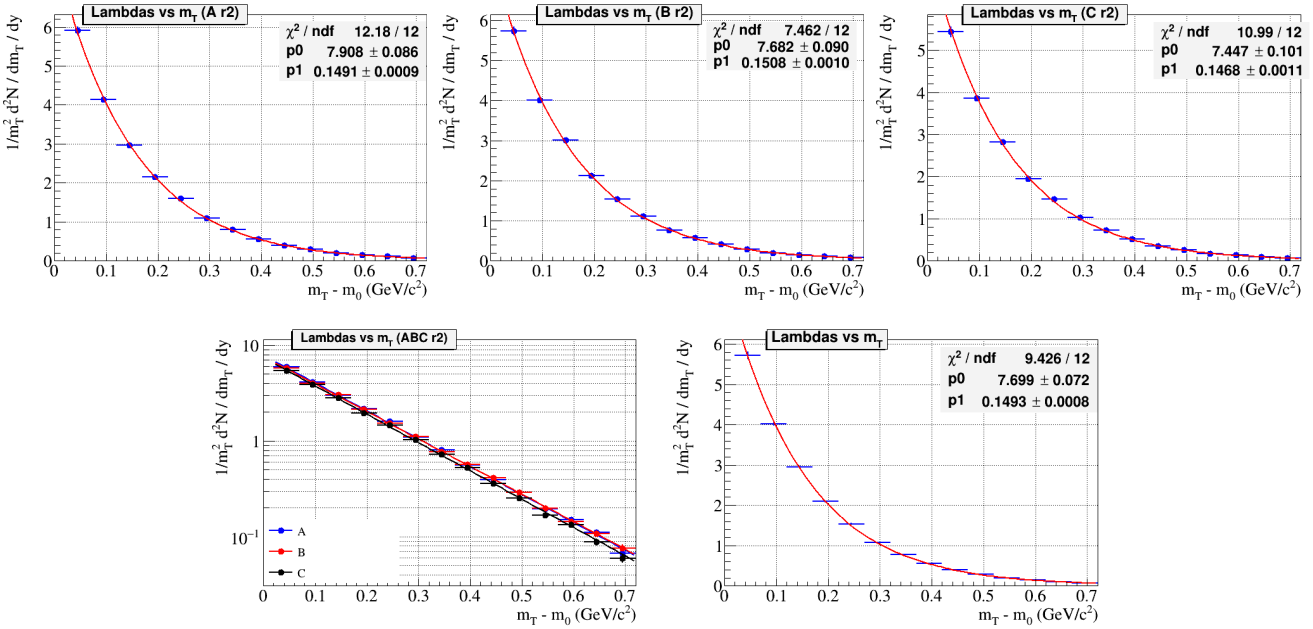

Figure 25: Λ hyperon transverse mass spectra. Upper row from left to right: event samples A, B, C. Lower left: A, B and C samples superimposed. Lower right: combined statistics. 0-10% collision centrality, $0.3 < y_{CMS} < 0.5$.

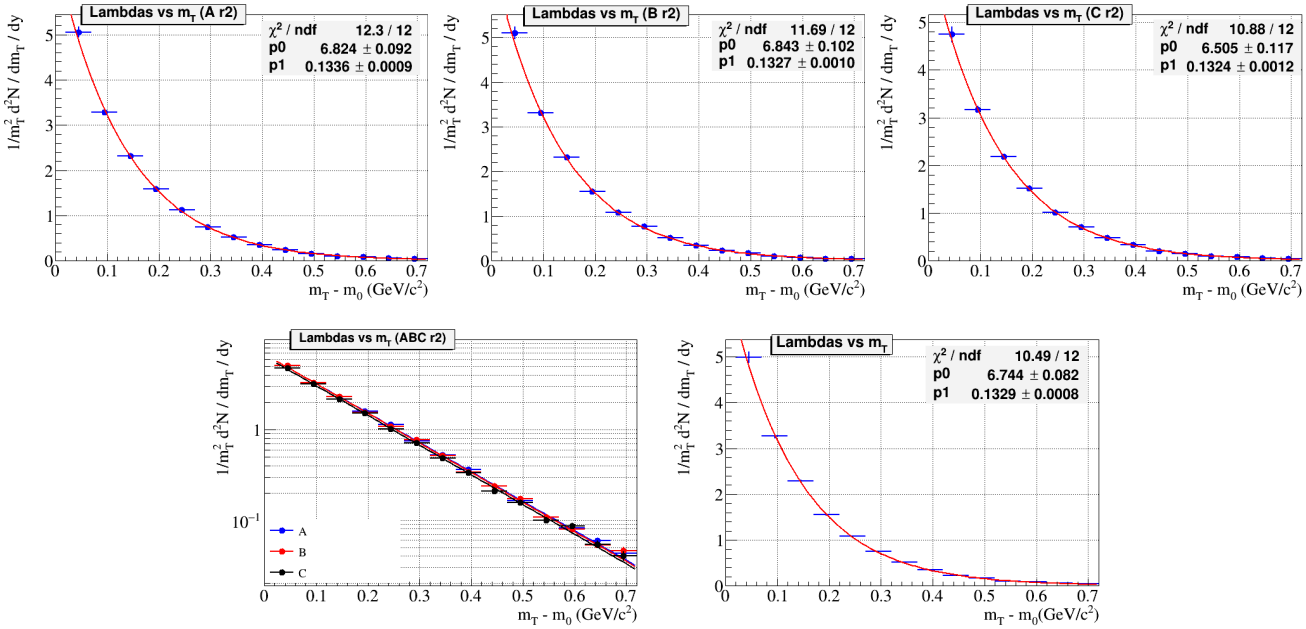

Figure 26: Λ hyperon transverse mass spectra. Upper row from left to right: event samples A, B, C. Lower left: A, B and C samples superimposed. Lower right: combined statistics. 0-10% collision centrality, $0.5 < y_{CMS} < 0.7$.

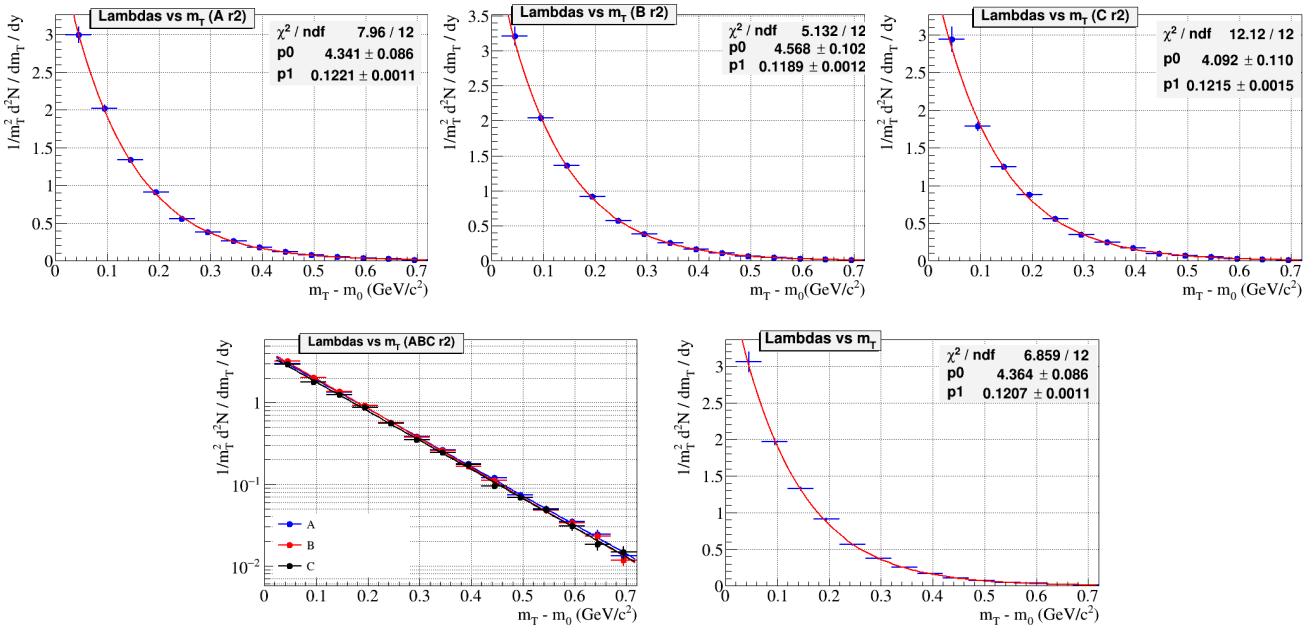

Figure 27: Λ hyperon transverse mass spectra. Upper row from left to right: event samples A, B, C. Lower left: A, B and C samples superimposed. Lower right: combined statistics. 0-10% collision centrality, $0.7 < y_{CMS} < 0.9$.

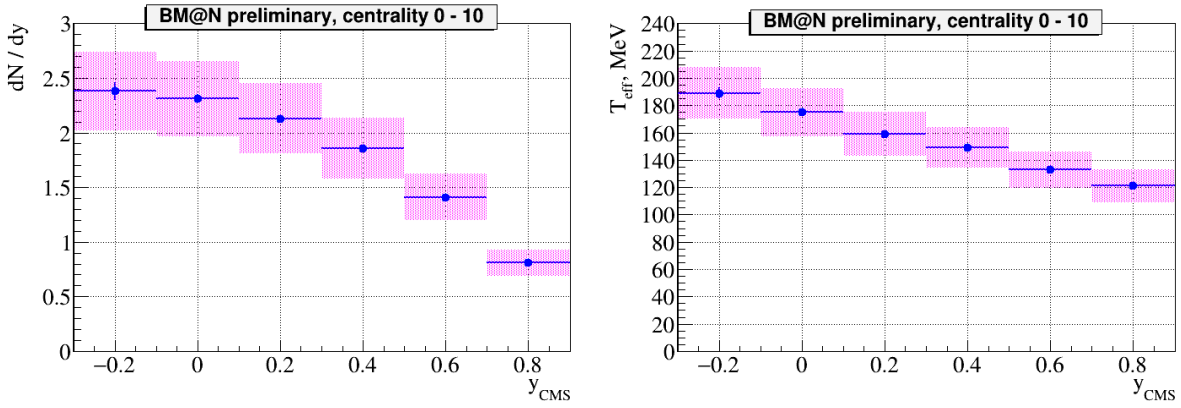

Figure 28: (Left) - rapidity spectrum of Λ hyperons; (right) - effective temperature as a function of rapidity. 0-10% collision centrality. Shaded rectangles represent systematic errors.

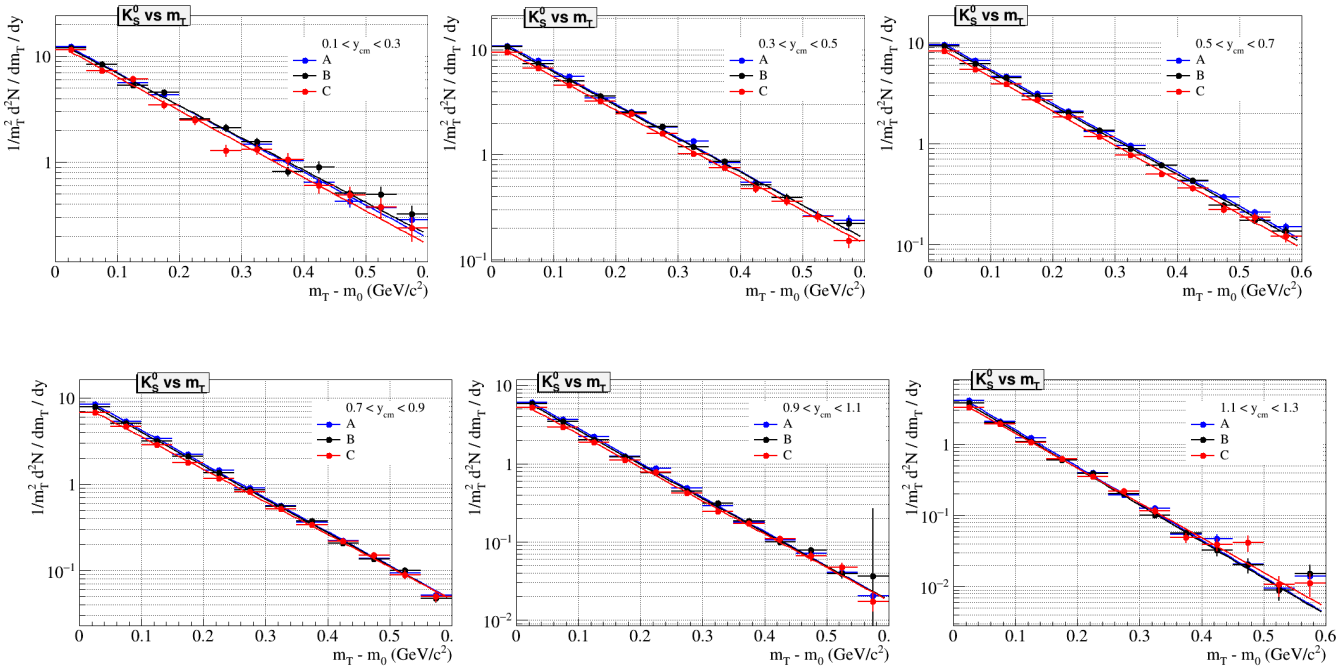

Figure 29: K^0_S meson transverse mass spectra in different rapidity bins for event samples A, B, C. 0-10% collision centrality.

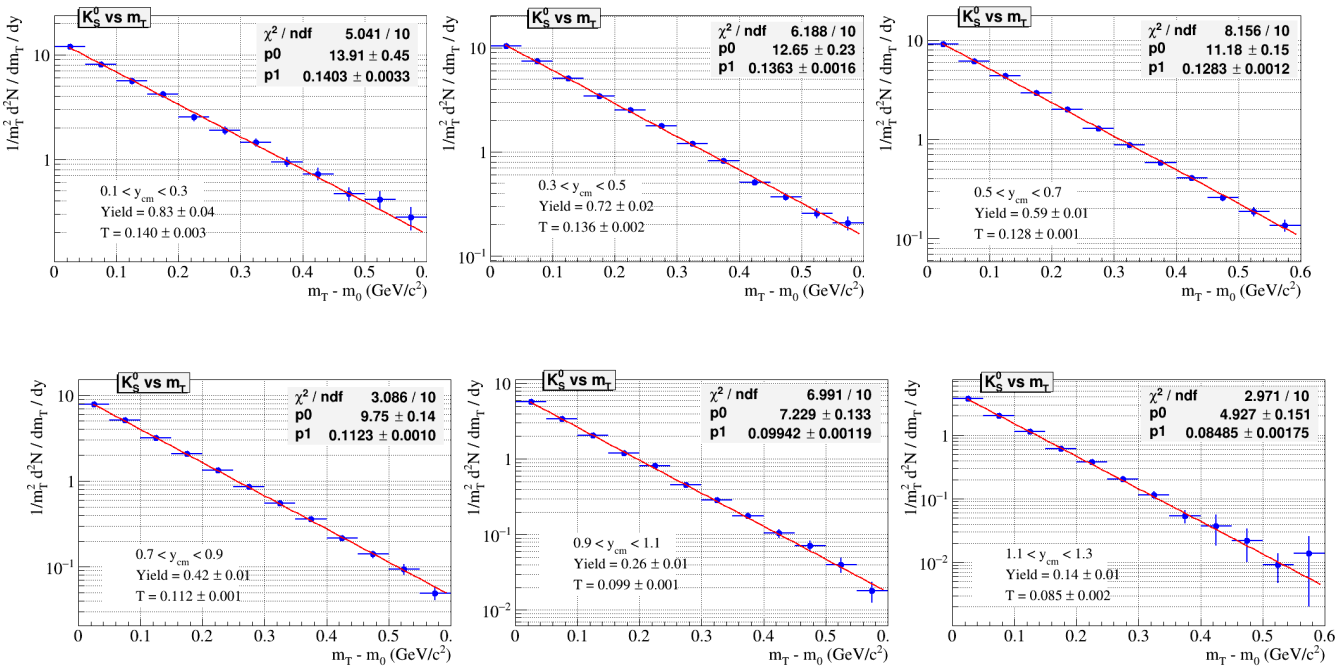

Figure 30: K^0_S meson transverse mass spectra in different rapidity bins for the combined statistics. 0-10% collision centrality.

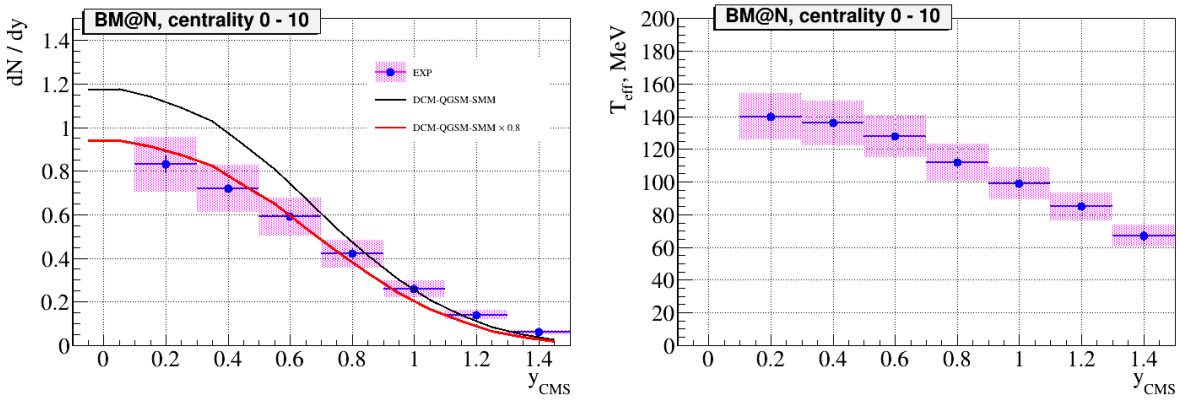

Figure 31: (Left) - rapidity spectrum of K^0_S mesons; (right) - effective temperature as a function of rapidity. 0-10% collision centrality. Shaded rectangles represent systematic errors. Lines show predictions of the DCSM-SMM model (original and scaled by a factor of 0.8).

8 Acknowledgments

Data processing was done on the HybriLIT heterogeneous computing platform (LIT, JINR) [20].

References

[1] P. Senger, "Studies of dense nuclear matter at NICA", [arXiv:2005.13856 [nucl-ex]]

[2] P. Senger, "Heavy-Ion Collisions at FAIR-NICA Energies", Particles **4**, no.2, 214 (2021)

[3] P. Senger, "Review of the BM@N Physics and Upgrade Program", Phys. Part. Nucl. **52**, no.4, 506 (2021)

[4] P. Senger, "Probing Dense Nuclear Matter in the Laboratory: Experiments at FAIR and NICA", Universe **7**, no.6, 171 (2021)

[5] V. Friese, "Prospects for the study of baryon-rich matter at new facilities", PoS **CORFU2018**, 186 (2019)

[6] M. Kapishin, "Studies of baryonic matter at the BM@N experiment (JINR)", Nucl. Phys. A **982**, 967 (2019)

[7] M. Kapishin *et al.*, "Production of hyperons, strange mesons and search for hypernuclei in interactions of carbon, argon and krypton beams in the BM@N experiment", Phys. Part. Nucl. **52**, 710 (2021)

[8] K. Redlich, A. Tounsi, "Strangeness enhancement and energy dependence in heavy ion collisions", Eur. Phys. J. C **24**, 589 (2002)

[9] S. Afanasiev *et al.* [BM@N Collaboration], "The BM@N spectrometer at the NICA accelerator complex", Nucl. Instrum. Meth. A **1065**, 169532 (2024)

[10] D. Zinchenko, E. Nikonov, A. Zinchenko, R. Zinchenko, "Development of the Vector Finder toolkit for track reconstruction in the BM@N experiment", Phys. Part. Nucl. Lett. **21**, no.3, 544 (2024)

[11] D. Zinchenko, A. Zinchenko, R. Zinchenko, E. Nikonov, "Development of a Vector Finder toolkit for track reconstruction at NICA experiments: current status and future prospects", Phys. Part. Nucl. **55**, no.4, 811 (2024)

[12] P. Batyuk, K. Gertsenberger, S. Merts, O. Rogachevsky, "The BmnRoot framework for experimental data processing in the BM@N experiment at NICA", EPJ Web. Conf. **214**, 05027 (2019)

[13] R. Luchsinger, Ch. Grab, "Vertex reconstruction by means of the method of Kalman filter", Comput. Phys. Commun. **76**, 263 (1993)

[14] S. Gorbunov, I. Kisel, "Reconstruction of decayed particles based on the Kalman filter", CBM-SOFT-note-2007-003. 7 May 2007. Available online: `https://www.star.bnl.gov/~bouchet/KFParticle/DOC-2007-May-14-1.pdf` (accessed on 15 November 2024).

[15] A. Zinchenko *et al.*, "A Monte Carlo Study of Hyperon Production with the MPD and BM@N Experiments at NICA", Particles **6**, no.2, 485 (2023)

[16] V. Kolesnikov, D. Suvarieva, V. Vasendina, A. Zinchenko, "Optimization of Techniques for Λ Hyperon Measurement at MPD/NICA," Phys. Part. Nucl. **55**, no.4, 827 (2024)

[17] M. Baznat, A. Botvina, G. Musulmanbekov, V. Toneev, V. Zhezher, "Monte-Carlo Generator of Heavy Ion Collisions DCM-SMM", Phys. Part. Nucl. Lett. **17**, no.3, 303 (2020)

[18] G. Agakishiev *et al.* [HADES Collaboration], "Hyperon production in Ar+KCl collisions at 1.76A GeV", Eur. Phys. J. A **47**, 21 (2011)

[19] M. I. Abdulhamid *et al.* [STAR Collaboration], "Strangeness production in $\sqrt{s_{\rm NN}}$ = 3 GeV Au+Au collisions at RHIC," JHEP **10**, 139 (2024)

[20] A. Anikina *et al.*, "Structure and Features of the Software and Information Environment of the HybriLIT Heterogeneous Platform", In: Vishnevsky, V.M., Samouylov, K.E., Kozyrev, D.V. (eds) Distributed Computer and Communication Networks. DCCN 2024. Lecture Notes in Computer Science, vol 15460. Springer, Cham. https://doi.org/10.1007/978-3-031-80853-1_33 (2025)

9 Supplementary material

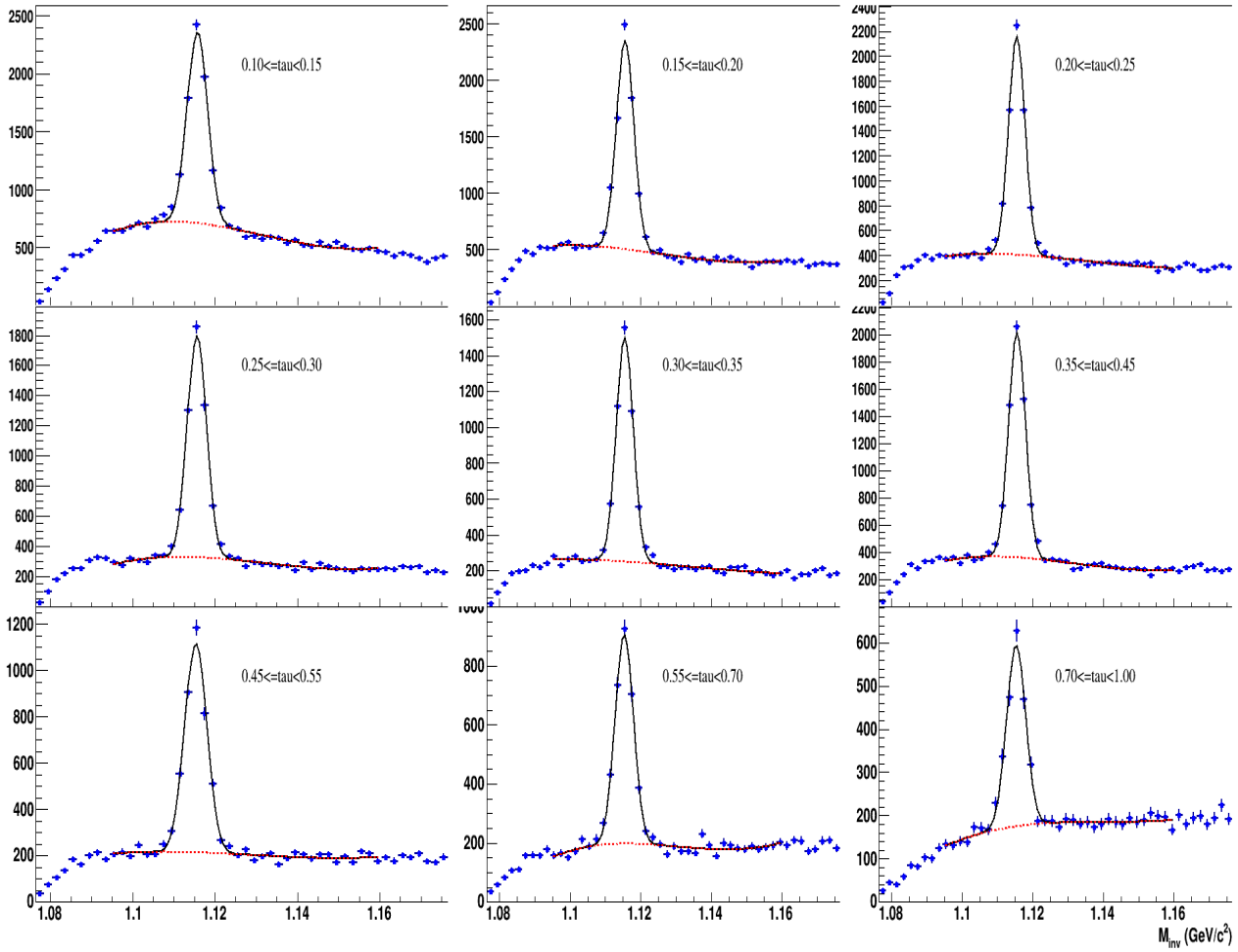

Figure 32: Invariant mass distributions of Λ candidates in 9 lifetime bins. $\sim$5 million events from runs 7830, 7873, 7876, 7877, 0.5*7878 were processed. Black solid lines show results of the fit to a sum of a gaussian and a 3-rd degree polynomial functions. Red dashed lines present the 3-rd degree polynomials.

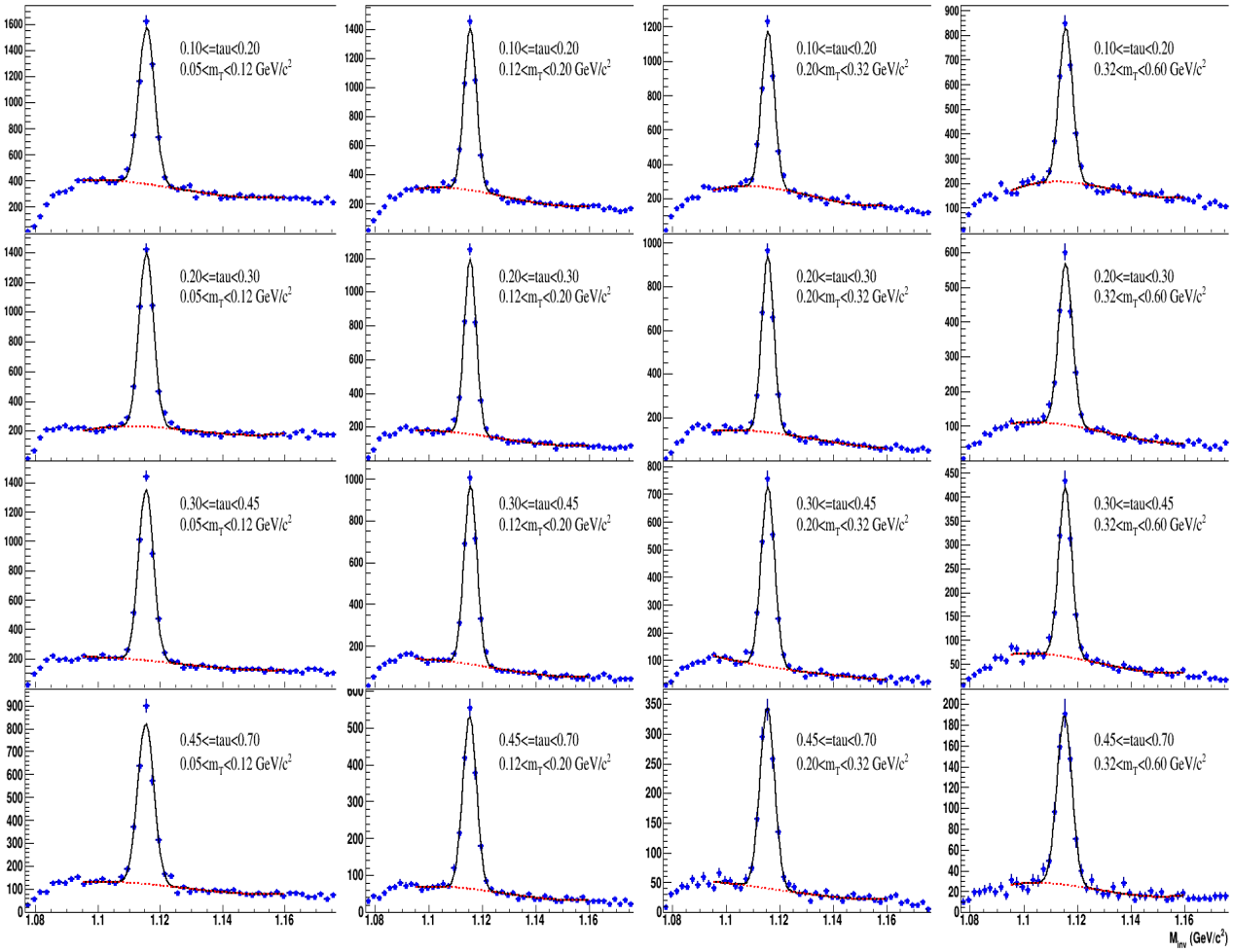

Figure 33: Invariant mass distributions of Λ candidates in $m_T - t$ bins. $\sim$5 million events from runs 7830, 7873, 7876, 7877, 0.5*7878 were processed. Black solid lines show results of the fit to a sum of a gaussian and a 3-rd degree polynomial functions. Red dashed lines present the 3-rd degree polynomials.

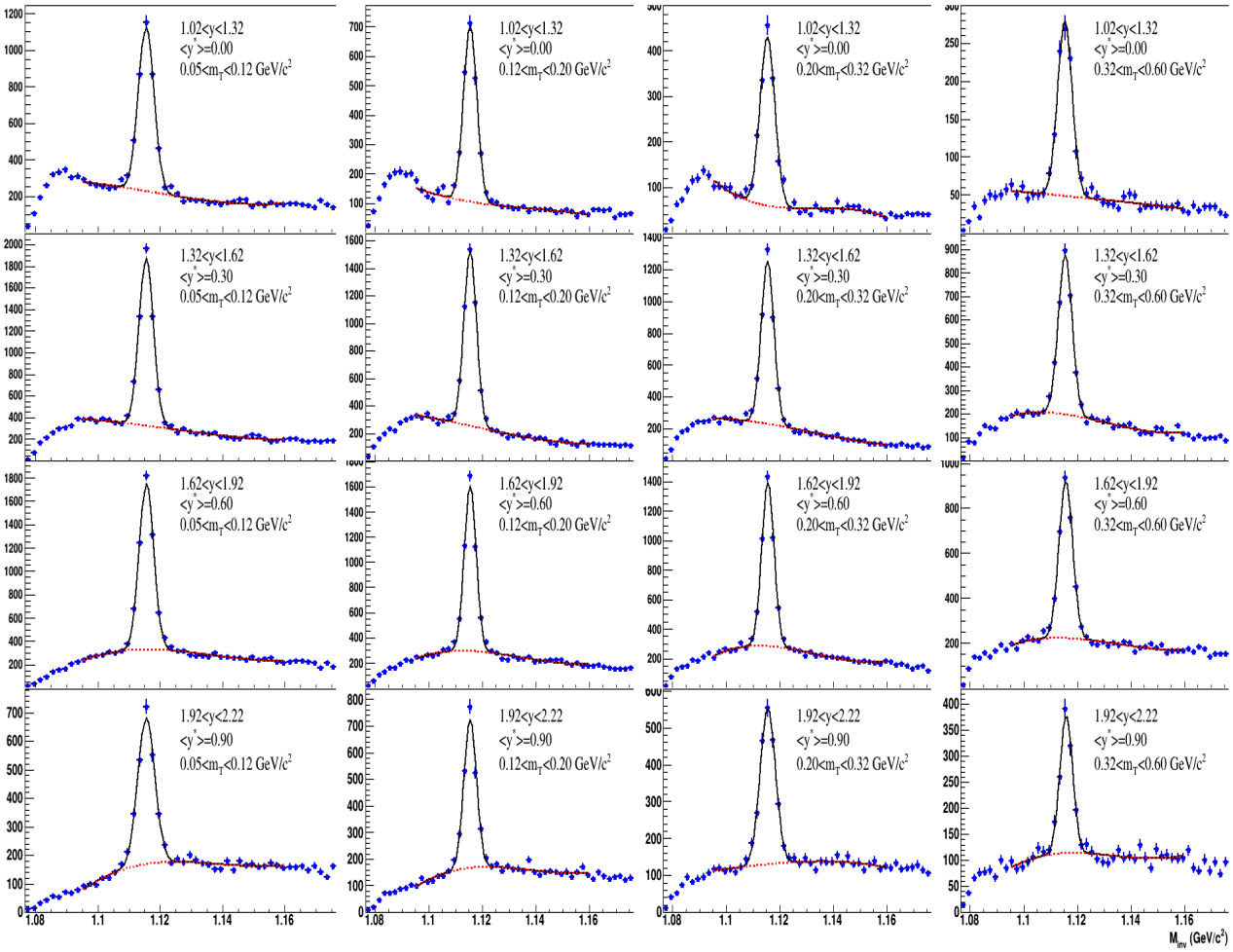

Figure 34: Invariant mass distributions of Λ candidates in $m_T - y$ bins. $\sim$5 million events from runs 7830, 7873, 7876, 7877, 0.5*7878 were processed. Black solid lines show results of the fit to a sum of a gaussian and a 3-rd degree polynomial functions. Red dashed lines present the 3-rd degree polynomials.

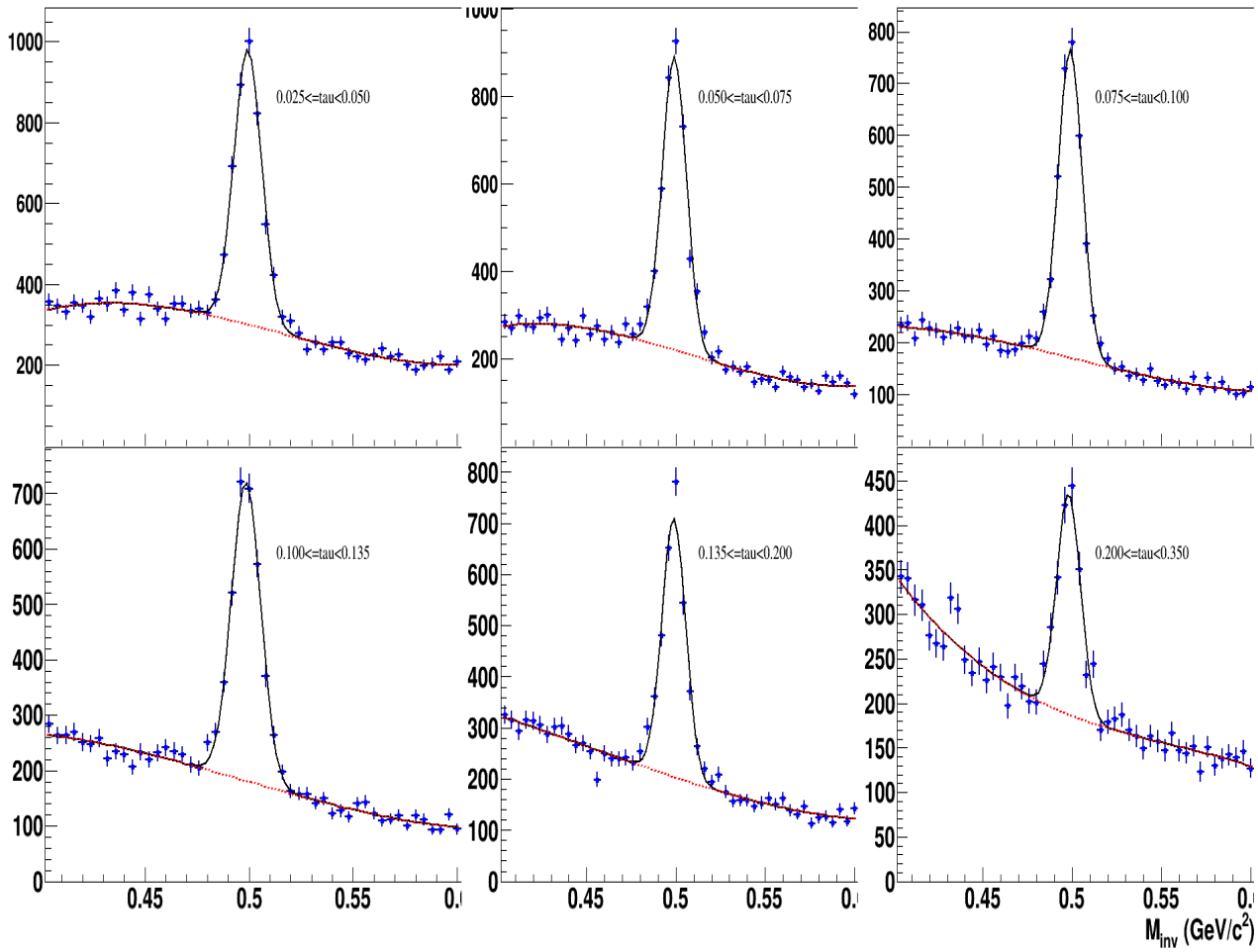

Figure 35: Invariant mass distributions of K^0_S candidates in 6 lifetime bins. $\sim$4 million events from runs 7830, 7873, 7876, 7877 were processed. Black solid lines show results of the fit to a sum of a gaussian and a 3-rd degree polynomial functions. Red dashed lines present the 3-rd degree polynomials.

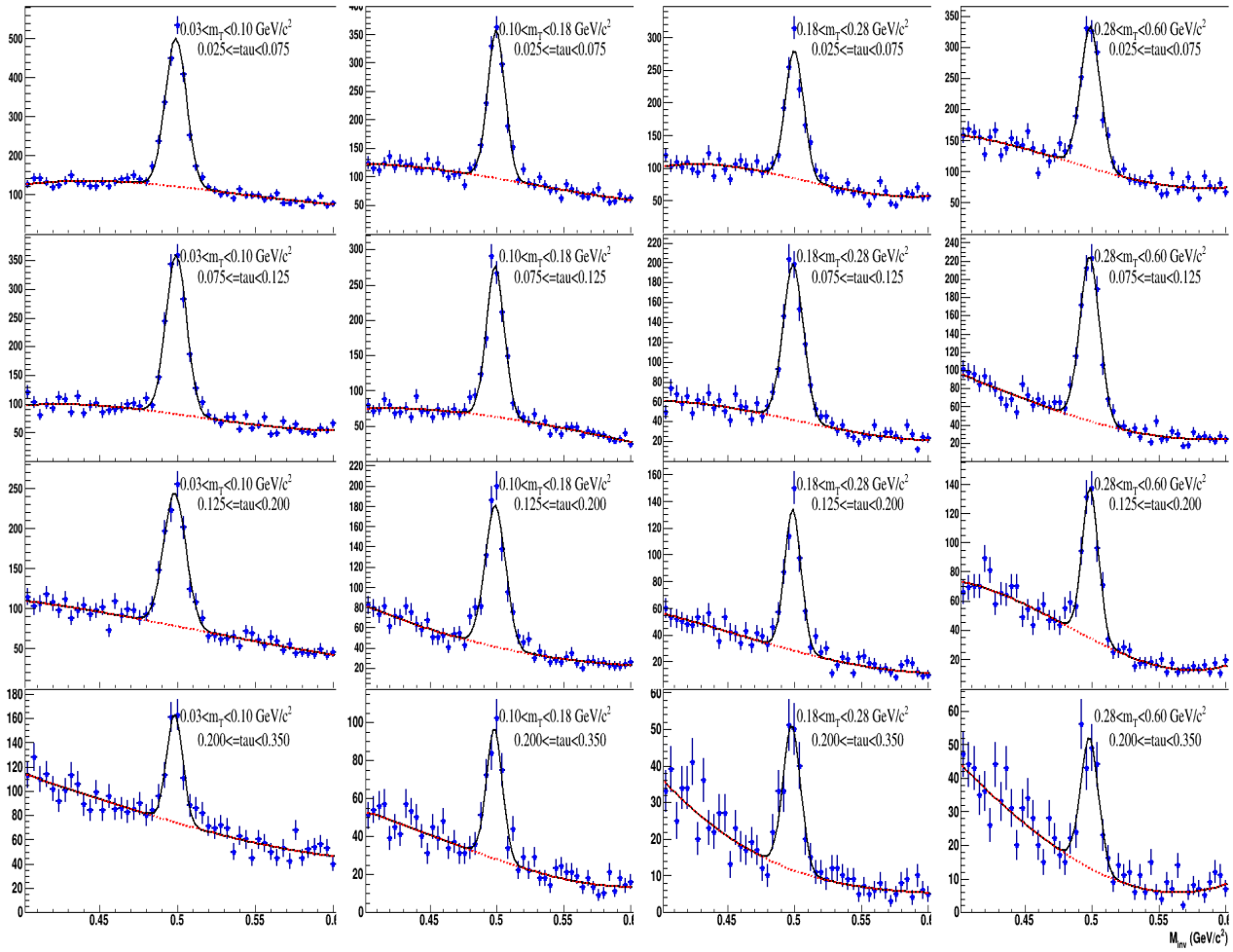

Figure 36: Invariant mass distributions of K^0_S candidates in $m_T - t$ bins. $\sim$4 million events from runs 7830, 7873, 7876, 7877 were processed. Black solid lines show results of the fit to a sum of a gaussian and a 3-rd degree polynomial functions. Red dashed lines present the 3-rd degree polynomials.

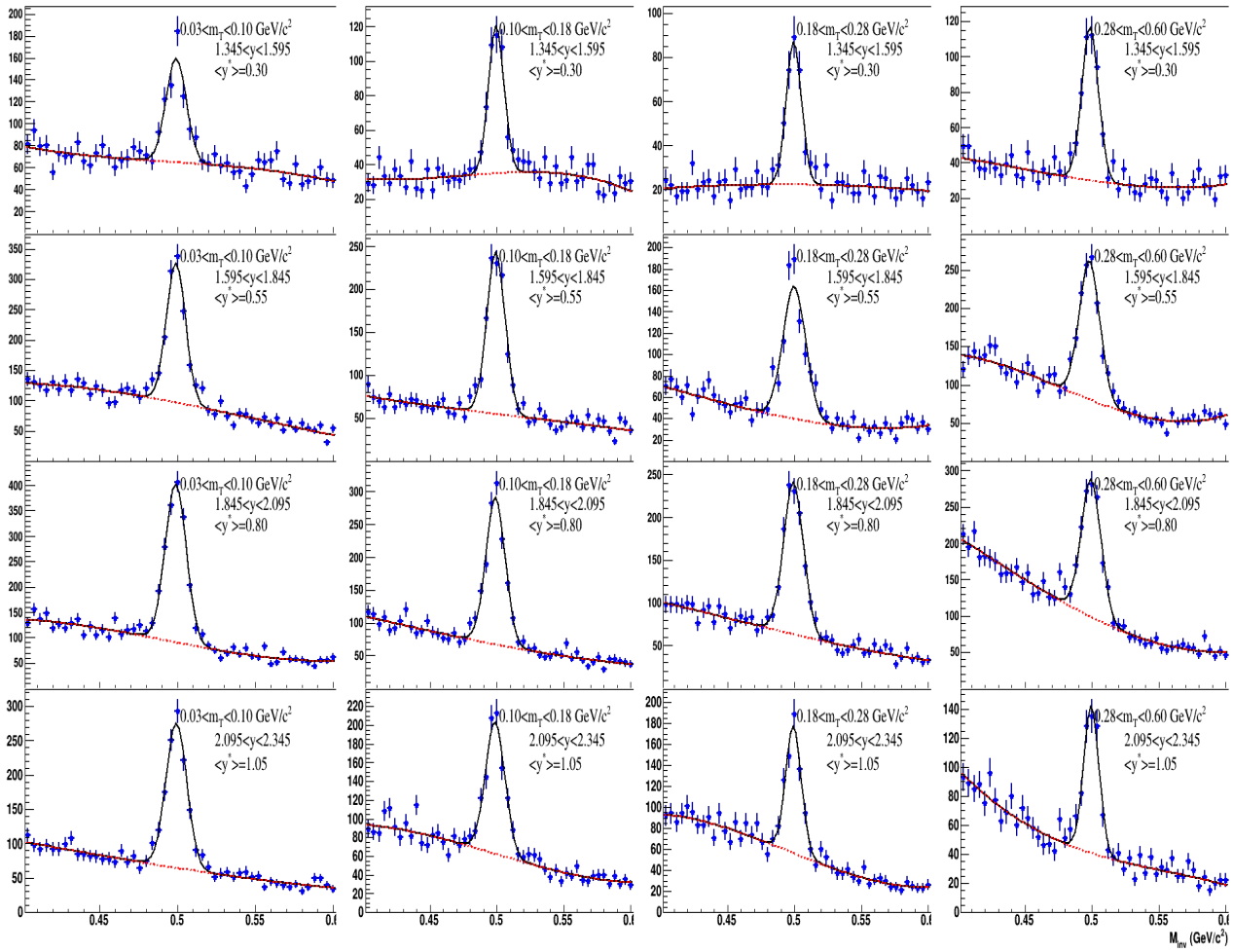

Figure 37: Invariant mass distributions of K^0_S candidates in $m_T - y$ bins. $\sim$4 million events from runs 7830, 7873, 7876, 7877 were processed. Black solid lines show results of the fit to a sum of a gaussian and a 3-rd degree polynomial functions. Red dashed lines present the 3-rd degree polynomials.